CHALMERS
UNIVERSITY OF TECHNOLOGY

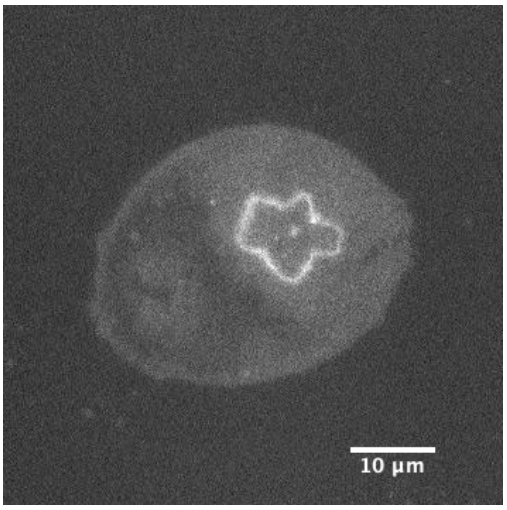

NIR-dye Based Heat Generation System for Studying Thermodynamic Response of Lipid-Bilayers

Master's thesis in Nanotechnology

LIN XUE

Department of Physics
Chalmers University of Technology
Gothenburg, Sweden 2019

MASTER'S THESIS IN NANOTECHNOLOGY

NIR-dye Based Heat Generation System for Studying Thermodynamic Response of Lipid-Bilayers

LIN XUE

Examiner: Mikael Käll

Supervisor: Steven Jones

CHALMERS
UNIVERSITY OF TECHNOLOGY

Department of Physics
Bionanophotonics
CHALMERS UNIVERSITY OF TECHNOLOGY
Gothenburg, Sweden 2019

NIR-dye Based Heat Generation System for Studying Thermodynamic Response of Lipid-Bilayers

LIN XUE

Supervisor: Steven Jones, Department of Physics
Examiner: Mikael Käll, Department of Physics

Master's Thesis 2019:NN
Department of Physics
Division of Bionanophotonic

Chalmers University of Technology
SE-412 96 Gothenburg
Telephone +46 31 772 1000

Cover: Fluorescence image of lipid film thermal migration on NIR dye doped PDMS substrate under the exposure of near-IR laser

Typeset in LaTeX
Printed by Chalmers Reproservice
Gothenburg, Sweden 2019

NIR-dye Based Heat Generation System for Studying Thermodynamic Response of Lipid-Bilayers

LIN XUE
Department of Physics
Chalmers University of Technology

Abstract

In this study, we develop a local heat generation system utilizing the photothermal effect on the micro-scale. Organic dye molecules are hosted in a polymer matrix to construct an NIR-absorbing medium, and it is proved to be an alternative candidate to plasmonic nanoparticles for creating a system with high absorption in the NIR regime and high transmission at visible wavelengths.

We carry out optical and thermal simulations to optimize the heat generation of such a system. The transfer matrix method is used to calculate the system absorption dependence on the NIR-absorber thickness and NIR dye concentration. It is shown that for a concentration of 5 mg/ml a 20 μm thick absorbing layer can provide 30% of absorption at 1064 nm, which is sufficient for generating an effective heat source density. In COMSOL multiphysics we obtain a simulation of the heat generation system in two configurations, indicating that the illumination with a NIR laser can provide sufficient heating.

It is valuable to study the micro-scale thermal migration and manipulation of biological particles in a temperature gradient, since it can provide the information on the interaction between the molecules and the solvent. Therefore, based on our NIR-absorbing system, we present several experiments investigating the thermodynamic response of lipid-bilayers. It is found that the local heating can facilitate the formation of lipid-bilayers from fluidic phase adsorbed vesicles. This might result from the promotion of vesicle rupture and the consequent fusion between lipids leading to the formation of a bilayer. Another study utilizing the lipid phase transition demonstrates that a photobleached spot within a gel phase lipid-bilayer can only recover in the presence of NIR-laser heating causing the local temperature to increase above the transition threshold. Adopted from this observation, we establish a reversible gel phase lipid lithography system, which utilizes a visible laser and NIR laser as a pen and eraser, respectively, to be able to optically print a desired pattern on the canvas made of lipid materials and then thermally remove it.

Keywords: NIR dye, optical absorption, photothermal effect, lipid-bilayers, lipid phase transition.

Acknowledgements

During my master thesis project in Chalmers, I have been given a taste for doing research, and have received a lot of help and assistance from the brilliant minds I worked with.

Firstly, I am profoundly grateful to my supervisor Steven Jones, who always patiently guides me and gives me tremendous suggestions on every detail. Secondly, I would thank my examiner Mikael Käll for his inspiration to begin this project and professional consultation in all the time. At the same time, my heartfelt thanks go to all the members in Bionanophotonics division for their appreciated aid, Timur Shegai, Ruggero Verre, Hana Jungová, Battulga Munkhbat, Partha Patrim Patra, Aili Maimaiti, Thomas Green, Betül Kücüköz, Daniel Andrén, and Adriana Canales Ramos. And because of them, I have great pleasure doing my thesis project in the past eight months.

Also, my sincere thanks to Fredrik Höök, Björn Agnarsson and Silver Jõemetsa from Biological Physics division, for providing the lipid materials as well as spin-on glass, and their enthusiastic advising in the experiments. In particular, I would thank Xinjian for his valuable interpretation on the molecule mass spectrum, and thank Alessandro Magazzù for his considerate help with sample preparation in UV-vis spectroscopy measurement. And I am deeply grateful to Philip Dalsbecker since I gain the experiences of polymer spin coating from him.

I owe my deepest gratitude to irep Gözen since I found the enthusiasm of working with lipids from her and her works. I would like to thank Emma Feldt for being my opponent and giving the comments on my thesis. Also, I thank Joakim Andreasson for giving the useful advices on dye absorption. Finally, I truly thank my family and friends for their endless support and encouragement during these two years I stayed in Sweden.

Lin Xue, Göteborg, September 2019

Contents

List of Figures

List of Tables

1
Introduction

In the realm of life science and bionanotechnology, studies on the migration of biological particles along temperature gradients on the micro-scale have recently attracted significant attention. These studies can provide a better understanding of the interaction between the biomolecules and the solvent, and the molecular binding process[1, 2]. The biological particles that have been studied involve DNA[3, 4, 5, 6], phospholipid membranes[7, 8, 9, 10], proteins[11, 12], and individual cells[13].

To microscopically generate temperature gradient, one common and effective approach is to utilize the photothermal effect induced by a focused laser beam into an absorbing medium[14, 15]. The drawback of using high power UV/visible lasers is that they can cause irreversible damage in the biological samples. However, biological samples have their minimum optical absorption in the NIR regime i.e. the "biological window" (650 to 1350 nm)[16, 17, 18, 19]. Therefore, NIR lasers are a promising tool to carry out such temperature gradient generation[20, 21, 22].

Apart from the NIR laser beam, an absorbing agent is necessary to convert optical energy into thermal energy in the photothermal effect. The metallic plasmonic nanostructure is an efficient absorbing agent due to the plasmonic resonance, and their resonance wavelength can be tuned to a specific wavelength within the visible or NIR region[23, 17, 24]. However, plasmonic nanostructures also provides some significant drawbacks. Plasmonic structures are not versatile since an appropriate design is fabricated before the experiment, and they can only provide a discrete heat source density due to their discrete physical nature. Also, plasmonic nanostructure will affect the emission from fluorophores or scatterers, consequently perturbing the system being observed.

Within the NIR regime, there are other commonly used absorbing agents, including semiconductor-based and carbon-based materials. Carbon-based materials such as amorphous carbon, carbon nanotubes, and graphene, exhibit relative broadband absorption ranged from UV-vis to infrared. This can be regarded as a disadvantage in selective spectral absorption applications[25, 26, 27], due to the undesired absorption of the visible light commonly used for fluorescent detection. Therefore, a system that can create versatile heat source density utilizing NIR absorption, while simultaneously being transmissive to visible wavelengths is highly desirable.

Organic semiconductors, with a conjugated polymer structure where π-electrons can delocalize, are competitive candidates for NIR absorption due to their relatively high absorbance as well as low-cost. Well developed conjugated polymers

including polyaniline[28], polypyrrole, and polydopamine[29, 30], are typically used as photothermal agents. In particular, being transparent in visible light and having relatively high absorption in the NIR regime would be the criteria for the dye molecules to establish the desired light-to-heat conversion system. This is due to the fact that in certain cases, a NIR laser is used to generate local heating and simultaneously a visible light source is used for fluorescent illumination in observing labeled biological samples. The advantage of using such NIR-dye based systems as alternative to plasmonic nanostructures is that they can avoid plasmonically enhanced fluorescence[31], strong scattering, and quenching. Additionally, the distribution of heat generation can be efficiently manipulated in real-time.

When the dye molecules concentrate and stack with each other, their absorption will alter due to intermolecular charge transfer. Therefore, a polymer matrix is needed to host and separate the dye molecules. Polydimethylsiloxane (PDMS), a silicon-based organic polymer, which is optical transparent in the visible light and NIR, has frequently been used for varied applications in the field of biotechnology such as for microfluidic channels and soft lithography[32, 33, 34]. It is reported that PDMS slab doped by visible dye has been developed and applied for on-chip fluorescence detection[35, 36, 37]. Compared with directly coating on a substrate, dispersing the dye molecules in PDMS matrix can achieve higher homogeneity as well as better control of dye-doped concentration, which is highly preferred in the optimization of the optical properties of an absorbing medium. Meanwhile, it has been proven that the absorption characteristic of the PDMS chip might differ from the dye dissolved in a solvent [35]. Hence, the way to combine NIR-dye with PDMS and the optical performance of such a system still requires study.

Artificial lipid-bilayers are a well studied standard system for mimicking the cell membranes that exist in most of living creatures[38, 39]. Under thermal effects, vesicles containing certain types of lipid molecules are known to exhibit various thermodynamic responses such as thermophoretic migration, domain partitioning and phase transition[8, 9, 40]. It is reported that a temperature gradient can be used to manipulate lipid nanotubes and trap lipid vesicles[7, 10]. Lene B. Oddershede and her co-workers demonstrated the direct qualification of local temperature increase by the lipid phase transition in the supported lipid-bilayers (SLBs)[41, 42, 43, 44]. Among these, the local heating is well defined by the plasmonic resonance of the nanoantennas, and thus it is interesting to associate the lipid bilayers phase transition with the photothermal conversion induced by the NIR-absorbed organic dye molecules. This is also expected in the application of NIR triggered liposome-encapsulated drug delivery systems[45].

This thesis aims to develop an optical system based on NIR-dye to generate temperature gradient induced by a NIR laser. Such a system is then used to carry out several experiments on lipid-bilayers formation and lipid phase transition. The layout for each chapter is list below:

In Chapter 2, the basic concepts related to optical absorption in bulk materials are introduced, and the origin of NIR-absorbance in dye molecules is explained. Also, the mechanisms of heat transfer in the photothermal effect are demonstrated. In the end, the self-assembly of lipid vesicles and SLBs formation

are described, followed by the explanation of the lipid phase transition from the gel phase to the fluidic phase.

In Chapter 3, optical and thermal simulations are presented to optimize the performance of the heat generation system. After that, the fabrication details of our NIR-absorbing thin film system are given. Finally, the methods used in the optical characterization of the heat generation system and the experimental setup concerning the lipid-bilayers experiments are exhibited.

In Chapter 4, the results from optical characterization and optical and thermal simulation of the heat generation system are shown. Most importantly, two different studies using fluidic phase and gel phase lipids, respectively, are discussed. The first study explores the promoted lipid-bilayers formation and the diffusivity of the formed bilayers on the PDMS substrate. The second study investigates the lipid phase transition and the thermal manipulation of the gel phase lipids.

The last chapter summarizes the discoveries in this thesis and gives suggested improvements and potential applications.

2

Theory

2.1 Bulk Material Optical Properties

In order to characterize the optical properties of NIR-dye molecules and the bulk material made from these dye molecules, the related theory and concepts used in the method section are introduced here including the absorption in dielectric media, Beer-Lambert law, the molecular absorption in NIR-dye molecules and the reflection at a planar boundary.

2.1.1 Absorption in Dielectric Media

When a electromagnetic wave propagates in a linear, nondispersive, homogeneous medium, the dielectric medium will create a polarization density $\mathcal{P}$ in response to an applied electric field $\mathcal{E}$[46]. If the medium is isotropic, the vectors $\mathcal{P}$ are parallel and proportional to the vectors $\mathcal{E}$ at every time as well as position, i.e.

$$\mathcal{P} = \epsilon_o \chi \mathcal{E} \tag{2.1}$$

where the constant ϵ_o is the electric permittivity in the free space and the scalar constant χ is the electric susceptibility of the medium. The electric permittivity ϵ is defined as

$$\epsilon = \epsilon_o(1 + \chi) \tag{2.2}$$

and $\epsilon/\epsilon_o = 1 + \chi$ is the relative permittivity of such a medium. Derived from Maxwell's equations, the speed of light in this medium can be written as

$$c = \frac{1}{\sqrt{\epsilon\mu}} \tag{2.3}$$

where μ is the magnetic permeability of the medium. Consequently, the refractive index n is defined as the ratio between the speed of light in free space and in the medium:

$$n = \frac{c_o}{c} = \sqrt{\frac{\epsilon}{\epsilon_o}\frac{\mu}{\mu_o}} \tag{2.4}$$

where μ_o is the magnetic permeability of the free space. If the material is nonmagnetic then $\mu = \mu_o$ and

$$n = \sqrt{\frac{\epsilon}{\epsilon_o}} = \sqrt{1 + \chi} \tag{2.5}$$

This relation indicates that the index of refraction is the square root of the relative dielectric constant. The complex refractive index can be denoted as

$$n = n' + i\kappa \tag{2.6}$$

where n' and κ are the real and imaginary part of refractive index, respectively[47]. A plane wave $E = E_0 exp(j\frac{2\pi}{\lambda}z)$ with a amplitude E_0 is transmitting through such a medium in the z-direction with the potential change in magnitude and in phase. Since $\lambda = \lambda_0/n$ where λ_0 is the wavelength in free space, the exponential term $j\frac{2\pi}{\lambda}z$ can be replaced by $-\frac{1}{2}\alpha z - j\beta z$, where β describes wave propagation and α describes the attenuation of the electric field as it propagates. The propagation constant β is defined as $\beta = nk_0$, where $k_0 = \omega/c_0$ is the wavenumber in the free space. The attenuation coefficient α is given by

$$\alpha = \frac{4\pi\kappa}{\lambda_o} \tag{2.7}$$

and a positive attenuation coefficient corresponds to absorption in the medium. Therefore, the intensity of the original plane wave $|U|^2$ decays by the factor $|exp(-\frac{1}{2}\alpha z)|^2 = exp(-\alpha z)$ as it propagates through the medium.

The relation between the total transmittance T, absorbance A, and the attenuation coefficient of a medium can be described by

$$T = \frac{\Phi_t}{\Phi_i} = e^{-\alpha z} = 10^{-A} \tag{2.8}$$

where Φ_t and Φ_i are the radiant flux transmitted and received by that medium, respectively[48].

2.1.2 Beer-Lambert Law

When a non-absorbing medium contains absorbing species i with a molar absorption coefficient ε_i, the imaginary part of the refractive index κ and thus the attenuation coefficient α of the whole material will alter from zero to a positive number. Assume the total number of the included absorbing species i to be N and the concentration of the included species to be $c_i = \frac{n_i}{N_A}$, where n_i and N_A are number density and Avogadro's constant, respectively. Through a light beam path length of l in the material sample, the absorbance A of such system can be described as

$$A = \sum_{i=1}^{N} \varepsilon_i \int_0^l c_i(z)dz \tag{2.9}$$

In the case of uniform concentration of the attenuating species, this expression could be simplified as

$$A = \varepsilon c l \tag{2.10}$$

Notice that the molar absorption coefficient ε has the unit [$M^{-1}cm^{-1}$] and the absorbance is unitless. Such linear dependence of the absorbance on the concentration of attenuating species is known as Beer-Lambert law. Notice that it is only

valid when the concentration is relatively low; otherwise, the molecules close to each other and the consequent interactions will break the linearity[49]. Combined the Beer-Lambert approximation and equation 2.8, we can directly relate the attenuation coefficient with the absorbance by

$$\alpha = -\frac{1}{l} ln(-\varepsilon cl) \tag{2.11}$$

The attenuation coefficient, or absorptivity, linearly depends on the concentration of the included species when the concentration is relatively low.

2.1.3 The Origin of the NIR Absorption of Organic Conjugated Molecules

The light absorption of conjugated molecules, or organic semiconductors, is dominated by the optical bandgaps of such molecules, which is the energy difference between the highest occupied molecular orbital (HOMO) and the lowest unoccupied molecular orbital (LUMO). Absorption occurs only when the photon energy is consistent with this optical bandgap, and based on Planck–Einstein relation $E = h\nu = hc/\lambda$, a narrower bandgap leads to the red shift of the spectrum i.e. to longer wavelengths. The backbone of aromatic molecules mainly consists of σ-bonds and π-bonds. The σ-bonding results from sp or sp^2 hybridization of atomic orbitals, whereas the π-bond is formed by the overlapping of p_z orbitals which are perpendicular to the σ-skeleton[50]. For example, in benzene molecules, the p_z orbitals indicated as a spindle in figure 2.1 a with opposite sign in the top and the bottom, are perpendicular to the hexagon hydrocarbon plane where the sp^2 hybrids orbitals are placed on. Figure 2.1 b shows the simplified model delocalized molecular orbitals when the same sign p_z orbitals overlap with each other, saturated above and underneath the σ-bonding plane. The establishment of π-bonds simultaneously creates a conjugated system within which π-electrons can freely delocalize.

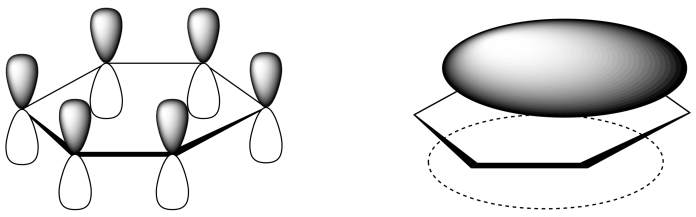

(a) **(b)**

Figure 2.1: (a) Illustration of p_z orbitals in a benzene molecule. (b) Illustration of the simplified de-localization of molecular orbitals in-phase

According to the fundamentals of quantum mechanical confinement i.e. the model of a one-dimensional quantum potential well, the expansion of a π-conjugated chain gives rise to a shrinking of the energy bandgap. Theoretically, the electronic structure of molecules, including potential energy of HOMO and LUMO can be

accurately simulated by density functional theory (DFT) utilizing the spatially dependent electron density.

The pigment molecule used in this study is $C_{62}H_{92}N_6Sb_2F_{12}$ (N3,N3,N6,N6-Tetrakis[4-(dibutylamino)phenyl]-1,4-cyclohexadiene-3,6-diaminium hexafluoroantimonate (1:2)), which has been applied for NIR laser protection[51]. The chemical structure is illustrated in figure 2.2. It is comprised of the cation part and anion part, and the conjugated system exists in the cation. Bonded nitrogen atoms, which have lone pairs of electrons indicated as black dots in figure 2.2, attached to the chromophoric substructures act as an auxochrome. As such, two identical chromophoric fragments that are linked together in a single molecule results in extending the π-conjugated system and lowering the energy bandgap of such system by intramolecular charge resonance (ICR)[52, 53]. Figure 2.3 depicts the resonance structure of such a cation and the grey area on the right side of the figure represents the conjugated system. It is reported that such a cation has its maximum absorption at 1090 nm in CH_2Cl_2[54], and the derivatives from its family have been used in the application related to the optical recording media.

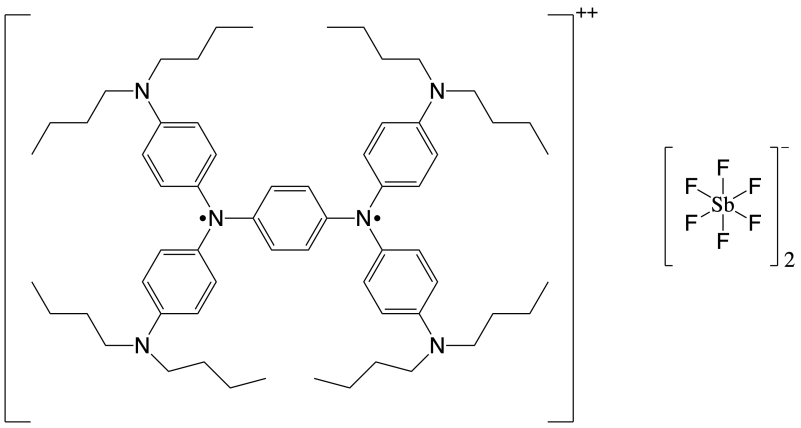

Figure 2.2: Illustration of chemical structure of the NIR-dye molecule

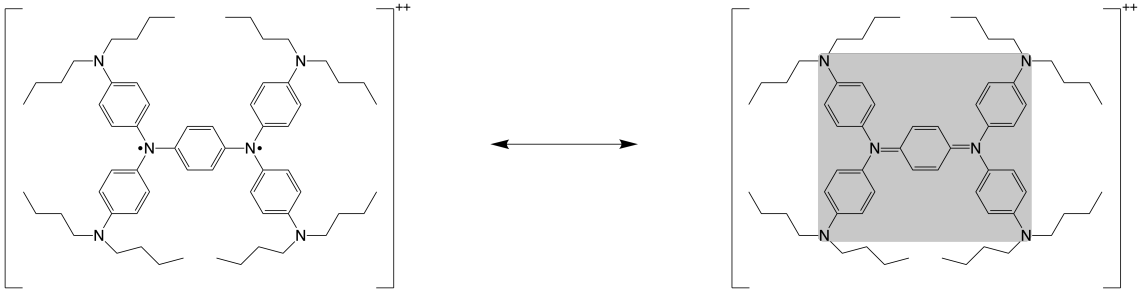

Figure 2.3: Illustration of the resonance structure of cation of the NIR-dye molecule

2.1.4 Reflection at a Planar Boundary

An incident plane wave with an arbitrary polarization is reflected and refracted at the planar interface of two dielectric media with refractive index n_1 and n_2,

and the incident, refracted and reflected angles are θ_1, θ_2 and θ_3, respectively, as demonstrated in figure 2.4. The plane in which the electromagnetic wave propagates before and after the reflection and refraction is called the plane of incidence. The x-polarized mode with its electric field perpendicular to the plane of incidence is denoted as s-polarization or transverse-electric (TE) polarization, whereas the y-polarized mode with its electric field parallel to the plane of incidence is denoted as p-polarization or transverse-magnetic (TM) polarization. The complex amplitude reflectances for the TE and TM polarization r_x and r_y are given by

$$r_x = \frac{n_1 cos\theta_1 - n_2 cos\theta_2}{n_1 cos\theta_1 + n_2 cos\theta_2} \tag{2.12}$$

$$r_y = \frac{n_1 sec\theta_1 - n_2 sec\theta_2}{n_1 sec\theta_1 + n_2 sec\theta_2} \tag{2.13}$$

For the case of normal incident, $\theta_1 = \theta_2 = 0$ so that $r_x = r_y = r$. Therefore, the power reflectance for both TE and TM polarization is given by

$$\mathcal{R} = |r|^2 = (\frac{n_1 - n_2}{n_1 + n_2})^2 \tag{2.14}$$

The power transmittance is then given by $\mathcal{T} = 1 - \mathcal{R}$.

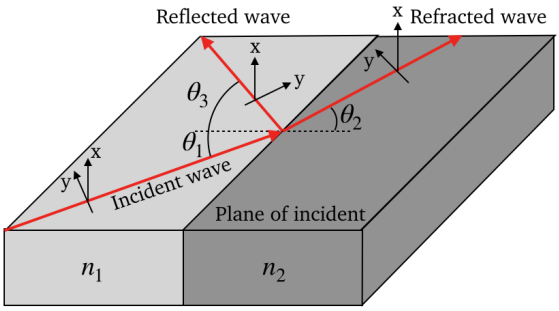

Figure 2.4: Illustration of reflection and refraction at the interface of two dielectric media with different refractive index

2.2 Heat Transfer

Heat transfer is a thermal non-equilibrium phenomenon that determines the rates of energy transfer between two systems resulting from their temperature difference. In general, the mechanism of heat transfer can be classified into three modes: conduction, convection, and radiation. Conduction is the transfer of energy between two contact particles with energy difference and can occur in solids, liquids, or gases. Particularly, the conduction in liquids and gases originates from collisions as well as the diffusion of randomly moving molecules. Convection, however, is the energy transfer resulting from fluid motions. Convective transfer can be induced by buoyancy forces or external surface forces, known as natural convection and forced convection, respectively. Thermal radiation occurs through

a vacuum or any transparent medium (solid or fluid or gas), and it is the transfer of energy in the form of electromagnetic waves or photons, and it occurs without any intervening medium.

Thermal radiation is significant only if the temperature difference between the two objects is huge, or one of the object is incredibly hot compared with the room temperature. Hence, heat transfer through thermal radiation can be neglected in terms of photothermal effect with limited laser power.

To determine whether the heat transfer is dominated by thermal conduction, we need to introduce the Rayleigh number Ra, which is the ratio of the time scale of thermal conduction to the time scale of natural thermal convection. It has the form in

$$Ra = \frac{g\beta\Delta T L^3}{\nu\alpha} \tag{2.15}$$

where g is the gravitational acceleration(g=9.8 m/s^2), β the coefficient of volume expansion (β=2.14$\times 10^{-4}$ 1/K for water at 20°C), ΔT the temperature difference between the interface and the ambient environment (ΔT=100 K), L the characteristic length of the geometry (1 μm<L<10 μm), ν the kinematic viscosity of the fluid (ν=1.004$\times 10^{-6}$ m^2/s for water at 20°C) and α the thermal diffusivity (α=0.143$\times 10^{-6}$ m^2/s for water at 20°C)[55].

For this study, we are considering the heat transfer from the polymer matrix, which is the heat source, to water. As the characteristic length is in the range from 1 to 10 μm, the Rayleigh number is approximated in the order of 10^{-6} to 10^{-3}, which is much smaller than 0.1 indicating the heat transfer by conduction is dominant[23].

Fourier's law of heat conduction states that the rate of heat transfer through a material is proportional to the negative gradient in the temperature and to the area, written as:

$$q = -k\nabla T \tag{2.16}$$

where q is the local heat flux density, k the thermal conductivity of the material and ∇T is the temperature gradient across the characteristic length. Materials with high thermal conductivity are able to conduct heat more efficiently over space than materials with low thermal conductivity, leading to a smaller temperature gradient for a given heat flux density. For example, silicon-based organic polymer PDMS has a thermal conductivity of 0.16 $Wm^{-1}K^{-1}$, which is much lower than silica glass(1.38 $Wm^{-1}K^{-1}$) and water (0.598 $Wm^{-1}K^{-1}$ at 20°C). Such inefficient thermal dissipation gives rise to the intense temperature increase on the polymer surface, as one of the advantages of this light-induced heat generation system.

2.3 Phospholipid Membrane

Phospholipids are amphiphilic biomolecules and they are the major component of cell membranes. The hydrophobic tails of lipid molecules consist of fatty acids, and the hydrophilic head is made by a phosphate group. An example is given in figure 2.5 b showing the chemical structure of 1-palmitoyl-2-oleoyl-glycero-3-phosphocholine (POPC) lipid molecule. By self-assembly, lipids are able to form

different architectures including lipid vesicles (liposome) and SLBs. The SLBs exhibit interesting two-dimensional fluidity and therefore they are widely used as an artificial soft material in biophysical experiments.

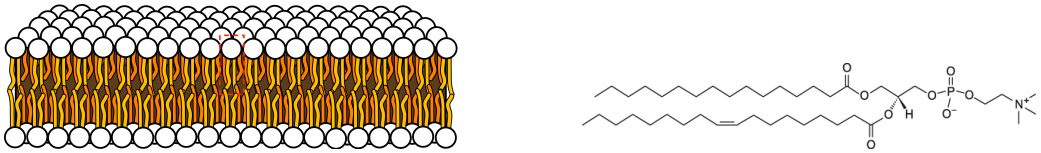

(a) **(b)**

Figure 2.5: (a)Illustration of artificial lipid membrane (b) Chemical structure of 1-palmitoyl-2-oleoyl-glycero-3-phosphocholine (POPC) lipid molecule.

2.3.1 Self-assembly of Lipid Vesicles and Supported Lipid-bilayer Formation

When lipid molecules are surrounded by water molecules in an aqueous environment, they tend to spontaneously organize their hydrophilic heads contacting with the aqueous solution to minimize the entropy, forming liposome- or micelle-like compartments. The transformation from lipid vesicles to SLBs can be described in three steps i.e. vesicle adsorption, vesicle rupture, and lipid-bilayers formation[56], as demonstrated in figure 2.6. The lipid vesicles in the solution (figure 2.6a) adsorb to substrate surface (figure 2.6b), followed by the consequent rupture of bound vesicles (figure 2.6c). Eventually the SLBs patches are formed and expand (figure 2.6d).

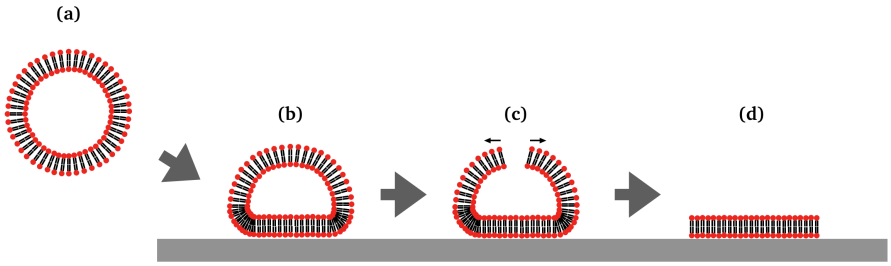

Figure 2.6: Illustration of supported lipid-bilayer formation. (a) Lipid vesicle in aqueous solution. (b) Adsorption of vesicle on solid substrate. (c) Rupture of adsorbed vesicle. (d) Formation of lipid-bilayer patch.

The lipid-bilayers are approximately 5 nm thick and there is a thin liquid layer existing between the bilayer and the substrate. The structure of the assembled lipid film depends on the type of deposited materials. In general, substrates with high surface energy (e.g., glass), promote the formation of lipid single/-double bilayer while low surface energy substances e.g., hydrophobic polymer, would facilitate the establishment of lipid monolayers[57]. As it will be introduced below, the native PDMS, the most commonly used silicon-based organic polymer, can lower its surface energy and becomes hydrophilic through oxygen

plasma treatment where the hydrocarbon groups replaced by silanol groups on the PDMS surface[58]. However, the hydrophobicity of plasma treated PDMS could recover and the recovery time depends on the environment[59]. Therefore, oxidized PDMS has been proven to be an alternative platform to support lipid-bilayers[60], and its temporal stability has been investigated[61].

2.3.2 Lipid Phase Transition

The phase transition temperature is one of the important properties of lipid-bilayers, describing how the relative mobility of individual lipid molecules changes with the environment temperature. Generally, there are two different phases of a lipid-bilayer i.e. gel (solid) phase and fluidic (liquid crystalline) phase. lipid-bilayers are constrained to the two-dimensional plane and in gel phase they have less lateral diffusivity whereas liquid phase lipids are able to diffuse more rapidly exchanging the location with their neighbors within the bilayers[62].

At temperatures above the characteristic phase transition temperature, lipids will undergo a transition from the gel phase to the liquid phase, and vice versa, as shown in figure 2.7. The transition temperature varies greatly from one to another type of lipid and is determined by both the attractive Van der Waals interactions between adjacent lipid molecules and the degree of unsaturation of the hydrophobic tails of the lipid[63]. A longer tail lipid has more area to interact with each other and thus, a higher strength of the interaction is gained. Also, lipid tails with an unsaturated double bond (e.g., DSPC lipid) in the alkane chain can produce a kink, disrupting the order of lipid packing and thus has a higher transition temperature than those with an only saturated tail (e.g., POPC lipid). This can also be read from their corresponding structure in figure 2.5b and 2.7b regarding the fact that transition temperature of POPC and DSPC lipid are -2^{o}C and 55^{o}C, respectively[64]. Consequently, lipid-bilayers that exist in the gel phase at room temperature can be used as an ideal tool to report the environment temperature change across its transition temperature and are thus a useful binary thermometer.

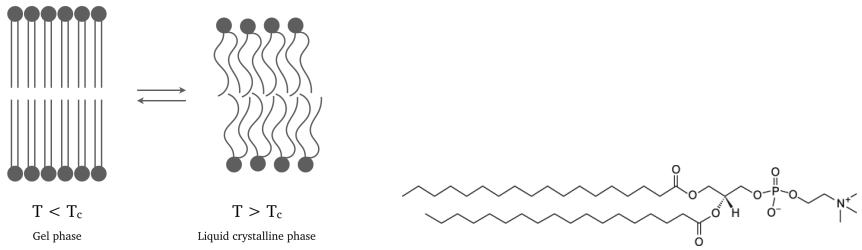

Figure 2.7: (a)Illustration of gel-to-liquid crystalline phase transition in a phospholipid-bilayer. T_c represents phase transition temperature.(b)Chemcial structure of 1,2-distearoyl-sn-glycero-3-phosphocholine (DSPC)

3
Methods

3.1 Optical and Thermal Simulations

Prior to practically fabricating the thin film heat generation system, an appropriate design which is able to provide sufficient local heating as well as an effective platform for studying biological samples is necessary. In this section, we introduce the optical and thermal simulation used to optimize the relative parameters involved in the process of NIR absorption within the absorptive polymer matrix and subsequent heat generation as well as transfer in the designed configuration, resulting in simulation of the resultant light-to-heat performance of our system.

3.1.1 Optical Simulation:Transfer Matrix Method

Our heat generation system consists of three stacked layers: water, polymer matrix doped with NIR-absorbing dye particles, and glass substrate, as illustrated in figure 3.1a. To simulate this system, we use transfer matrix method(TMM), since it can efficiently calculate the overall transmission, reflection and absorption for a multilayered system based on the Fresnel equations (equation 2.12 and 2.13). The explanations for normally incident light are given below.

A 2 by 2 transmission matrix **M** is introduced here to track complex amplitudes of forward and backward propagating plane waves through boundaries and homogeneous media[46]. This multilayer medium with prescribed thickness and refractive index can be conveniently divided into a series of basic elements $\mathbf{M}_1$, $\mathbf{M}_2$, ...,$\mathbf{M}_N$ (figure 3.1b). The **M** matrix for each element is calculated by its scattering matrix S using the Fresnel equation (2.12) and thus the corresponding M matrix is given by

$$\mathbf{M} = \begin{bmatrix} A & B \\ C & D \end{bmatrix} = \frac{1}{t_{21}} \begin{bmatrix} t_{12}t_{21} - r_{12}r_{21} & r_{21} \\ -r_{12} & 1 \end{bmatrix} \tag{3.1}$$

where r_{12} and t_{12} are the amplitude reflectance and transmittance coming from the left while r_{21} and t_{21} are the amplitude reflectance and transmittance incident from the right. In the case of propagation through a homogeneous medium, the **M** matrix is

$$\mathbf{M}_{propagation} = \begin{bmatrix} exp(ik_0nd) & 0 \\ 0 & exp(-ik_0nd) \end{bmatrix} \tag{3.2}$$

Meanwhile, the **M** matrix for a dielectric boundary between two media of refrac-

tive indexes n_1 and n_2 are given by the matrix:

$$\mathbf{M}_{boundary} = \frac{1}{2n_2}\begin{bmatrix} n_2+n_1 & n_2-n_1 \\ n_2-n_1 & n_2+n_1 \end{bmatrix} \tag{3.3}$$

Within the NIR dye-doped PDMS layer, the real part of its complex refractive index is assumed to be approximately the same as pure PDMS (n≈1.4), whereas the imaginary part is obtained from the corresponding absorptivity (equation 2.7). The overall transmission matrix **M** for the whole system is calculated by multiplying the M matrix for each elements: $\mathbf{M}=\mathbf{M}_N...\mathbf{M}_2\mathbf{M}_1$. Eventually, the total transmittance and reflectance is obtained by the scattering matrix that has the conversion relation:

$$\mathbf{S} = \begin{bmatrix} t_{12} & r_{21} \\ r_{12} & t_{21} \end{bmatrix} = \frac{1}{D}\begin{bmatrix} AD-BC & B \\ -C & 1 \end{bmatrix} \tag{3.4}$$

A, B, C and D are the elements in the M matrix. Transfer matrix method can principally apply to even more complicated systems with an arbitrary number of dielectric layers.

Utilizing transfer matrix method, we can fine-tune the system absorption at 1064 nm by varying the dye-loading concentration, corresponding to the absorption coefficient, and the thickness of the NIR-absorbing layer.

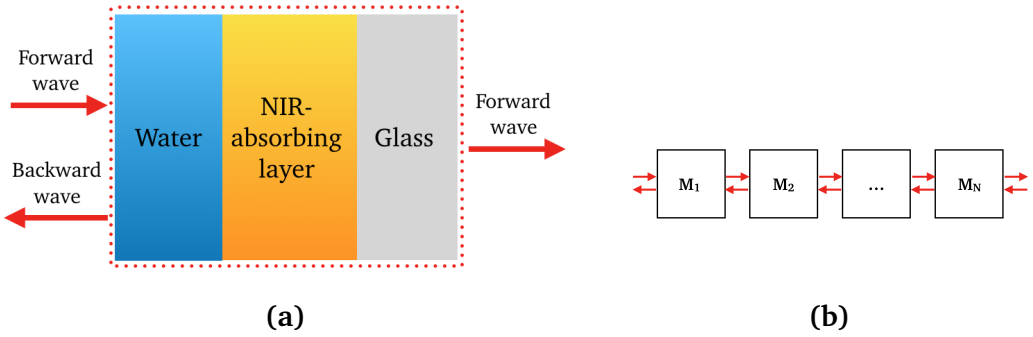

Figure 3.1: Illustration of wave-transfer matrix theory of multilayer optics

3.1.2 Thermal Simulation: COMSOL Multiphysics

Based on the optical simulation, the system absorption is determined, however, the thermal effect induced by NIR absorption is still to be quantified. Therefore, COMSOL multiphysics is used to thermally predict the temperature profile and geometry variation in this system. The numerical methods behind COMSOL are mainly the finite element method (FEM) which computes the approximation of the partial differential equations (PDEs) based upon discretizations.

In COMSOL, the simulated system includes glass substrate, PDMS layer (with or without spin-on glass layer on top), water and the cover slide, as indicated in figure 3.2. NIR-absorber consists of dye-doped PDMS is assigned to be the heat source density via the absorption of laser beam. The heat source density is defined

by

$$Q(r,z) = \frac{\eta P}{(2\pi)^{3/2}\sigma_r^2\sigma_z} exp(-\frac{(r-r_0)^2}{\sigma_r^2} - \frac{(z-z_0)^2}{2\sigma_z^2}) \tag{3.5}$$

where η is the absorption efficiency (%), P is the input laser power, r_0 the central radius position of the beam, z_0 the center position of the beam in z-direction, σ_r and σ_z the radius size and depth of the focus beam parameters, respectively[65]. Note that the exponential term represents the three-dimensional generalization of the Gaussian point spread function. Reasonable estimation of beam size and depth are selected to simulate the heat source density. The heat fluxes on the surface in contact with the air are simulated as external nature convection cooling, and the initial temperature of the ambient environment is set to be 293.15K (20°C). A fine mesh area and an appropriate mesh scale factor are assigned to resolve the Gaussian beam. A typical surface plot of the simulated temperature profile is shown in figure 3.2 in the scenarios with and without spin-on glass on top of the PDMS layer. The temperature distribution along the PDMS/water or glass/water interfaces (r in figure 3.2) along with the input laser power is simulated by parametric sweep study and shown in section 4.2.2.

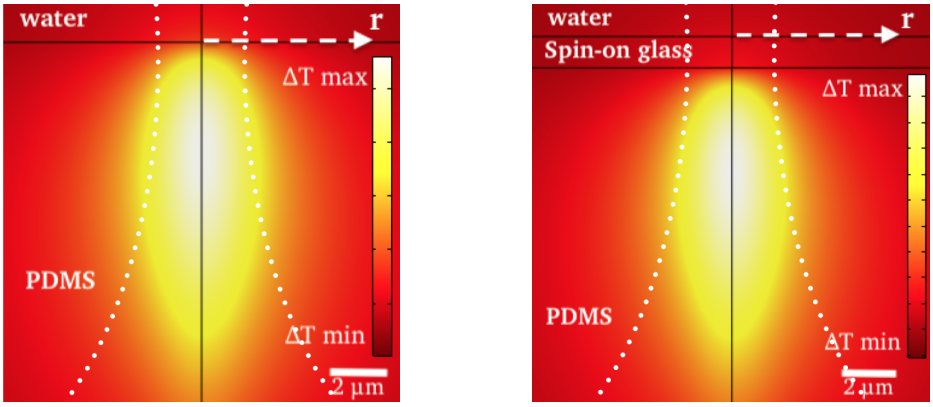

(a) **(b)**

Figure 3.2: Surface plot of the simulated temperature increase in the r-z plane in two different configurations. (a)water directly contact with PDMS layer. (b)Spin-on glass sandwiches between water and PDMS layer. Color scale bar represents the temperature increase (K) based on the room temperature (293.15K). The input laser power is 100mW. White dashed arrow indicates the radius distance and the dotted line indicates the laser beam profile.

3.2 NIR-absorbing Thin Film Fabrication

Based on the optimized design obtained from the optical and thermal simulations as mentioned above, the fabrication of the NIR-absorber thin layer in the heat generation system can be carried out in mainly four steps: surface preparation, incorporation of dye solution with PDMS, spin coating and finally sample curing. Meanwhile, the addition of spin-on glass on top of the system is an alternative

offering advantages included high stability and facilitating the formation of lipid bilayers.

Surface preparation is a crucial step to form a uniform topography of PDMS layer on top. A 170 μm thick circular glass substrate is rinsed with DI water, acetone, isopropanol and ethanol for 10 s each followed by the nitrogen drying.

The second step is to dope the PDMS with NIR-dye particles, and it is the most critical part in the fabrication process. In order to create spaces between the individual NIR dye molecules, a silicon based polymer PDMS is used as a matrix to host such particles, otherwise the stacking of the particles will alter their absorption due to the intermolecular interactions. It is also reported that the uniformity of dye-doping can be improved by adding the dye molecules into the solvent prior to mixing with PDMS monomer and catalyst, toluene and acetonitrile are utilized as the mediator[35]. The details of fabrication are given below. NIR dye (FT36492, Carbosynth) are dissolved respectively in 0.2 mL of toluene/acetonitrile, and the solution is then poured into 2 g of PDMS monomer with a weight ratio of 10:1 with the curing agent (Sylgard 184 Silicone Elastomer kit). The initial dye concentration is ranged from 1 to 20 mg/ml corresponding to 2-40 mg addition of the dye molecule. The mixture is vigorously stirred until a uniform color is obtained and degassed in vacuum for 30 min to remove the air bubbles.

Next, the deposition of a uniform thin dye-doped PDMS layer on glass substrate is achieved by spin coating technique, in which the substrate is rotated at high speed and the coating material is spread by centrifugal force. The degassed dye-doped PDMS is spin-coated on the clean glass substrate using the spin coater (WS-400-Lite series, Laurell Technologies) at 113 rpm/s acceleration speed for 60 s. The applied spin-coating speed varies from 1000 to 6000 rpm resulting in difference thickness of the fabricated sample. Finally, the sample is cured at 90°C in the oven (Memmert) for four hours to evaporate the solvent and facilitate the polymerization.

Spin-on glass fabrication is an alternative to modify the PDMS surface so that such heat generation system can be used in more applications and meanwhile, it acts as a protective layer. To fabricate such a layer, a butanol based coating solution (IC1-200, FUTURREX) is applied on cured PDMS surface and spin-coated at 6000 rpm for 60 s. Such a sample is then placed on the hot plate at 120°C for 30 min.

The final thickness of the spin-coated PDMS is determined by spin time and angular velocity[66]. Profilometry is then used to characterize the film thickness as well as surface topograph, and the result of a typical measurement is shown in figure 3.3 where the PDMS layer is fabricated under 3000 rpm/s speed for 60 seconds, resulting in around 21.5 μm. A set of experiments is carried out to quantify the relation between the thickness and the spin-coating speed, and the result is shown in table 3.1. By utilizing 1000 to 6000 rpm spinning speed for one minute, the thickness can be well controlled from 15 to 100 μm, and an even thinner layer can be obtained through a extended fabrication time. Notice that the central thickness is measured here and the deviation from the actual thickness($\pm 3\mu m$) is estimated based on the measured error and the variation among the samples, and this result closely agrees with the reference literature[67]. One factor that could

also influence the spinning process is the viscosity change of the uncured PDMS monomer mixed with the dye solution, and this originates from the swelling of the PDMS by the solvent (toluene/acetonitrile). In fact, it is observed that the dye-doped PDMS mixture exhibits an increase in viscosity after the incorporation of acetonitrile. In addition, there is no significant effect found on the optical performance of the fabricated PDMS chip contributed from the curing time and temperature.

Table 3.1: Thickness of spin coated PDMS and corresponding spin coating speed

Spin-coating speed (rpm)	Measured thickness (μm)	Reference thickness (μm)
1000	100 ± 3	77
2000	35 ± 3	36
3000	24 ± 3	28
4000	18 ± 3	19
6000	15 ± 3	12

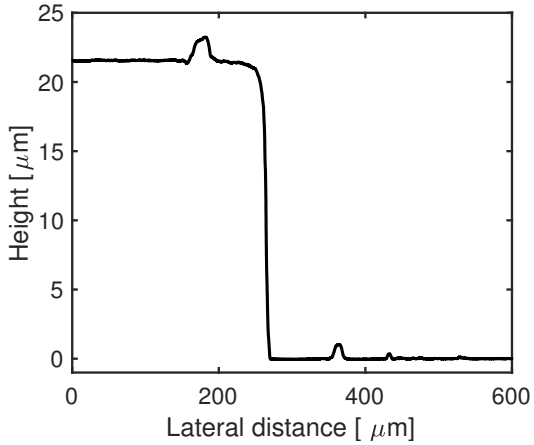

Figure 3.3: Plot of thickness of spin-coated PDMS layer measure by profilometry. The fabrication uses 3000 rpm spin-coat speed, 226 rpm/s acceleration speed and 60s spin-coat time.

3.3 Experiments

3.3.1 Ultraviolet–visible Spectroscopy and Mass Spectrometry

To optically simulate the heat generation system, the absorption coefficient of the absorptive materials is required. This can be quantitatively analysed by UV-vis spectroscopy, which is able to collect the absorption spectrum of the sample ranged from ultraviolet to NIR wavelength. The working principle is that a single wavelength beam emitted from the light source travel through the sample and the blank, and eventually arrive at the detector. The light-source automatically scans

through wavelengths in the UV-visible-NIR regime and the transmission spectrum is recorded. Based on equation 2.8 the absorption spectrum is therefore obtained.

In this study, we use UV-vis spectroscopy (Cary 5000, Agilent) to measure the absorbance of the dye-solvent solution and the transmission of the dye-doped PDMS chip. The wavelength scanning is carried out from 400 to 1600 nm at scanning speed 100 nm/min with 1 nm resolution. In the case of dye solution, the solvent is chosen to be the baseline and the sample concentration is 0.01 M whereas in the measurement of dye-doped PDMS the NIR-dye concentration is varied and a PDMS film of the same thickness with no dye molecules is used as the baseline.

To clarify, two types of dye molecules purchased from Fabricolorholding and Carbosynth are named as Dye A and B, respectively. The structure of Dye B has been discussed in section 2.1.3. In order to determine the chemical structure of Dye A, which is not provided by the supplier, and the similarity between Dye A and B, their molar masses are required. As one of the most reliable technique to determine molecular weight, mass spectrometry (6120 SQ MS with 1260 HPLC, Agilent) is used to measure the mass spectrum, a plot of intensity as a function of the mass-to-charge ratio, of these two molecules following a standard procedure. The mechanism initiate from ionization, followed by the separation of such ions based on their specific mass-to-charge ratio (m/z), and as a result the relative abundance of each ion type is recorded. The mass spectra of dye A and B are shown in figure A.1 in the appendix.

3.3.2 Optical Setup

To be able to observe the fabricated sample, which is almost transparent and very thin, a dark-field microscope is extremely suitable in this case since it only collects the scattered light from the sample resulting in an enhancement in the contrast. Darkfield images of the dye-doped PDMS sample is acquired using a Nikon ECLIPSE 80i microscope equipped with a Nikon S Plan Fluor ELWD 60X 0.7NA objective, a darkfield condenser and an Andor iXon EMCCD camera, as illustrated in figure 3.4.

In the experiment of thermal response of lipid-bilayers, the visualization of lipid molecules accomplished by using tagged fluorophores (rhodamine B), which can be excited by the certain wavelength of photon, combined with fluorescent microscopy. The typical experimental setup is illustrated in figure 3.4, as the configuration of lipid bilayers in the environment of the heating platform, is shown on the right side. The lipid vesicles can be deposited and adsorbed either on the dye-doped PDMS or the spin-on glass on top (only the spin-on glass configuration is shown in figure 3.4). A mercury halide lamp and a fluorescent filter cube (Nikon TRITC filter cube) are used to illuminate the sample, while a Cobolt Rumba 1000 1064 nm laser and a Vortran Stradus 532 nm laser are used to heat up the NIR-absorber and photobleach the fluorophores, respectively. Meanwhile, a dichroic mirror (Thor Labs DMSP1000R) enable the NIR laser and 532 nm laser/mercury lamp simultaneously be incident on the sample plane. The selective light path between the mercury lamp and the 532 nm laser can be realized by rotating an

intervening mirror, indicated as a dashed arrow in figure 3.4. In the gel phase lipid lithography, a computer-controlled piezo-electronic stage (Nano-ZS series, MCL.inc) is used to carry out the three-axis motion creating the photobleached pattern accurately.

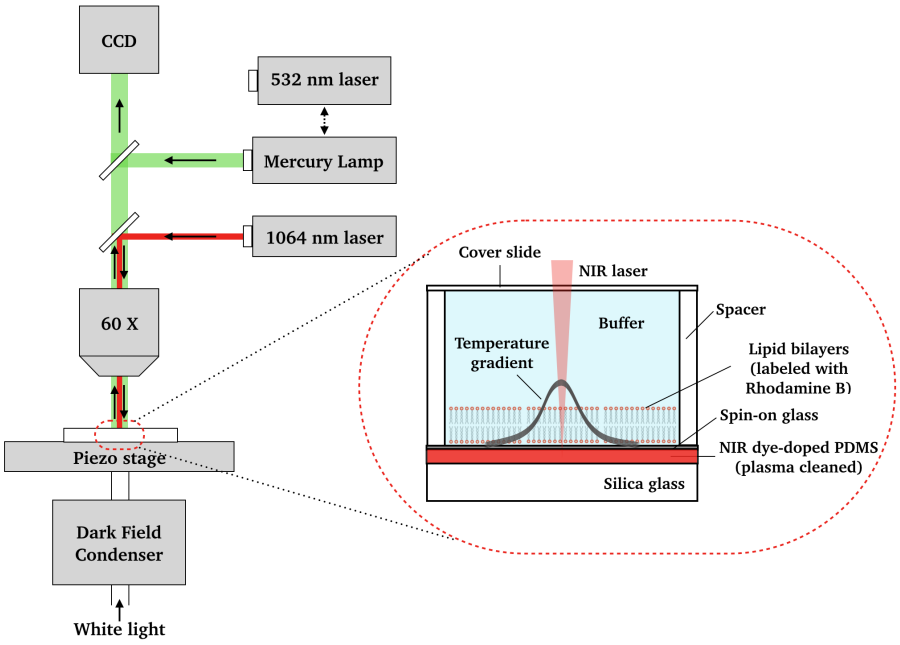

Figure 3.4: Illustration of the optical setup, including two set of lasers and mercury lamp, combined with the heat generation system. The detail of the sample is enlarged and shown on the right.

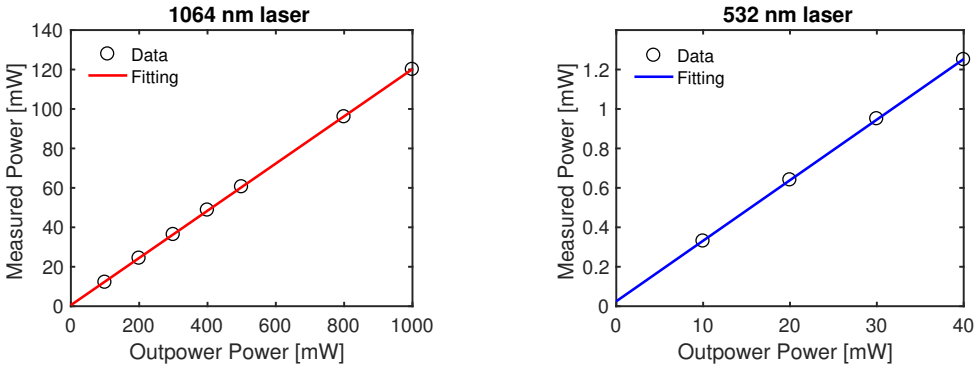

(a) **(b)**

Figure 3.5: The linear relation between the output power and the measured power at the sample plane. (a) the regression model for the 1064 nm laser is y=0.1197x+0.4243. (b) the regression model for 532 nm laser is y=0.0307x+0.0250.

Based on the fact that the optics in the beam path from the laser to the sample would significantly attenuate the laser intensity, it is necessary to correlate the output and actual power for both the 1064 nm laser as well as 532 nm laser.

The 1064 nm laser can output up to 1000 mW power intensity, and the intensity measured on the sample plane by a power meter (Thorlabs) exhibits linear dependence on the output power (figure 3.5a). The output power is roughly ten times higher than the measured power arrived at the sample. The operation power of 532 nm laser is ranged from 0 to 40 mW, its output power and measured power obey the similar trend by a reducing factor of 30, as shown in figure 3.5b. This significant attenuation is caused by the acousto-optic modulator (AOM) which is in the beam path of 532 nm laser. Unless specified, otherwise the laser power intensities mentioned below are all measured power.

3.3.3 Lipid Material Preparation and SLBs Formation

In general, there are two major phospholipids used in this study: the POPC lipid and DSPC lipid, which is in fluidic and gel phase in room temperature, respectively. In the encouraged supported lipid bilayers as well as fluorescence recovery after photobleaching, the lipid materials include POPC (16:0-18:1 PC : 1-palmitoyl-2-oleoyl-sn-glycero-3- phosphocholine), PEG2K PE (18:1 PEG2000 PE : 1,2-dioleoyl-sn-glycero-3- phosphoethanolamine-N-[methoxy(polyethylene glycol)-2000]) and Rhod PE (18:1 Liss Rhod PE : 1,2-dioleoyl-sn-glycero-3- phosphoethanolamine-N-(lissamine rhodamine B sulfonyl)). However, in the experiments concerned phase transition, POPC lipid is repalced by DSPC (1,2-distearoyl-sn-glycero-3-phosphocholine). All lipids are purchased from Avanti® Polar Lipids, Inc.

As the formation of supported lipid-bilayers is mentioned in section 2.3.1, the SLBs is self-assembled from lipid vesicle, and in this study, we use small unilamellar vesicles (SUVs). The preparation of SUVs suspensions follow the standard protocol[56, 68] by vesicle extrusion. The lipids with desired molar ratios are mixed and dissolved in chloroform (Sigma-Aldrich), followed by the evaporation in round bottom flasks facilitated by continuous nitrogen flow and vacuum overnight. Afterward, the TE buffer (125 nM NaCl (Sigma Aldrich), 10 mM TRIS (VWR) and 1 mM Na_2EDTA (Sigma Aldrich)) is used to rehydrate the dried lipid films, obtaining a lipid suspension in 1 mg/ml. A polycarbonate filter is used to extruded such lipid suspensions for more than ten times forming unilamellar lipid vesicles. All lipids vesicles are stored at 4°C in a refrigerator after the formation.

To be able to form the lipid bilayers on the PDMS, the dye-doped PDMS is plasma treated in a plasma cleaner (PDC-32G, Harrick Plasma) at high power for 5 min. Supported lipid bilayers formation is induced by vesicle attachment and rupture, as mentioned in section 2.3.1. The fluorescent unlabeled and labeled vesicles are mixed at a ratio of 100:1 in order to visualize the process of bilayers formation. In detail, a 2 μL suspension containing 100 μg/ml unlabeled (0.5 mol% PEG2K PE and 99.5 mol% POPC) and labeled vesicles (2 mol% Phod PE and 98 mol% POPC) is added onto the PDMS surface surrounded by the plastic spacer (100 μm thick, Thorlabs). After 10 minutes of self-assembly, the droplet is gently rinsed by 3 μL TE buffer using a pipette to eliminate the other vesicles in the solution.

4

Results and Discussions

In this chapter, the optical characterization of the fabricated NIR absorbing thin film is carried out, followed by the optimization of the heat generation and transfer by simulation. Moreover, the results from two studies associated with fluidic phase and gel phase lipid are presented and discussed.

4.1 Optical Characterization of NIR-absorbing Agent

The characterization of the optical performance of the NIR absorbing dye-based material consists of the absorption spectrum measurement and the dark field imaged of the fabricated sample for examining the overall quality of the fabricated sample.

The absorbance of 0.01 M NIR dye molecules A and B in three different solvents, toluene, acetone, and acetonitrile, were measured and normalized, as shown in figure 4.1. In figure 4.1b, the maximum and minimum values of the absorption spectrum in toluene, acetone, and acetonitrile appear at around 1064 nm and 600 nm, respectively, whereas an identical dip and a second highest peak at 1017 nm and 961 nm, respectively, are only displayed in toluene. Meanwhile, the spectrum in both acetone and acetonitrile show extreme similarity and gain their relatively high absorbance (>0.8) at a wavelength from 956 nm to 1123 nm.

As it is known that toulene is nonpolar solvent and acetone, as well as acetonitrile, are polar aprotic solvents, dye molecules A and B are high polarity molecules with positive charges within the conjugated system so that it can be dissolved well in acetone and acetonitrile. Therefore, due to the low solubility in toluene, part of the dye molecule may aggregate in the crystalline state, resulting in the splitting of the absorbance band in toluene.[54] Apart from the slight variations in the visible region, the absorbance spectrum of molecule B exhibits a similar trend as molecule A as introduced previously. Regarding the chemical structure of dye molecule A is unknown, the mass spectrum is measured to obtain the molar mass of these two dye molecules shown in figure 9A.1 in the appendix. It is suggested that both dye molecule contain the same cation with conjugated system which is responsible for the NIR absorption, resulting in their similar absorption spectra.

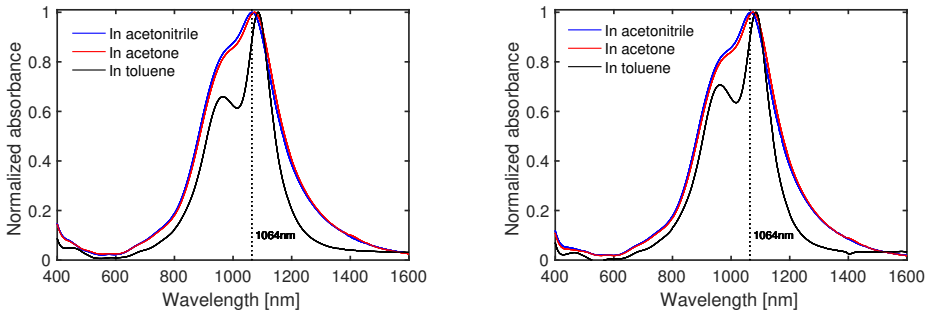

(a) Dye molecule A **(b)** Dye molecule B

Figure 4.1: Absorbance spectrum of NIR dye in acetonitrile (blue line), acetone (red line) and toluene (black line). Concentration is 0.01M.

It is well known that changing the host medium can cause significant changes to the absorption spectrum of dye molecules. Therefore the dye molecules were suspended in a PDMS host matrix using all three solvents. As can be seen from figure 4.2 when creating a PDMS-dye molecule compound using toluene as an intermediary the absorption spectra changes significantly. A qualitatively similar result was obtained when utilizing acetone. Meanwhile, if acetonitrile is used to transfer the dye molecules into a PDMS host matrix, the absorption maxima stays at approximately the same value although significant broadening of the absorption peak occurs (see figure 4.4).

Figure 4.2 shows the absorptivity per millimeter of a dye embedded in PDMS matrix mediated by toluene. A Savitzky-Golay filter has been applied to smooth the data. Dye concentration is varied from 1 to 5 mg/ml, and the measured thickness of the PDMS layer is 21.5 μm. A positive linear relationship can be seen between absorptivity and dye concentration when the dye concentration is relatively low, i.e. c=1-3 mg/ml. However, there is a dramatic boost of absorptivity when concentration is increased from 3 to 4 mg/ml, and the absorptivity tends to saturate at high concentration, i.e. c=5 mg/ml. Notice that the first and second highest peak in each concentration shift to 1300 nm and 858 nm, respectively, which is originally at 1085 nm and 961 nm in toluene environment. These could be explained that once the dye molecule reaches the saturated concentration in PDMS, crystallization process occurs leading to the nonlinearity of Beer-Lambert Law, which assume the absorbing media is homogeneous and does not scatter the incoming beam. In fact, once the solvent, e.g., toluene has been eventually evaporated, dye molecule can only exist in the solid-state in the polymer matrix, indicating that the light rays are completely absorbed by solid dye aggregates rather than by well-dispersed dye molecules. This agrees with the dark field image of the PDMS sample in the case that toluene act as solvent prior to blending with PDMS (figure 4.3), and it is clear that the size of crystals in different shapes increases with concentration, and dramatic enhancement can be observed particularly from c=3 to 5 mg/ml.

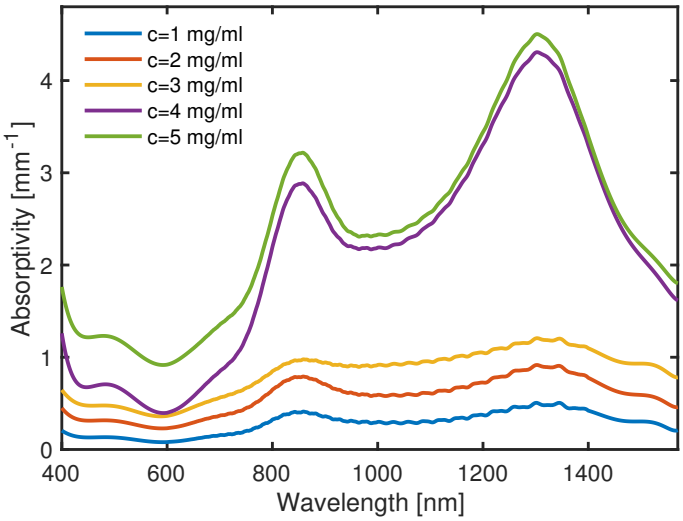

Figure 4.2: Ploting of absorptivity of the dye-doped PDMS mediated by toluene with dye concentration from 1 to 5 mg/ml. The raw data is smoothed by Savitzky-Golay filtering in MATLAB

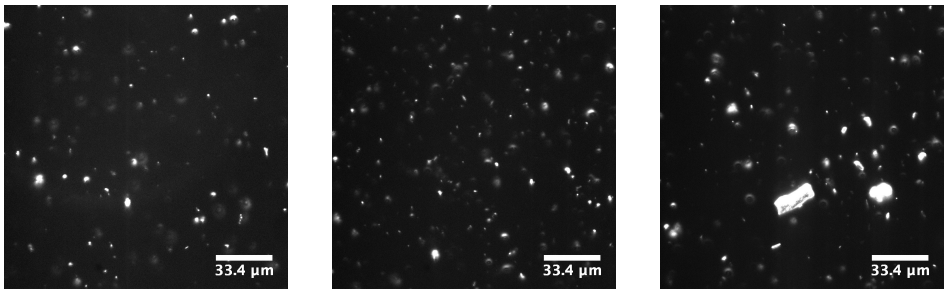

(a) c=1 mg/ml **(b)** c=2 mg/ml **(c)** c=3 mg/ml

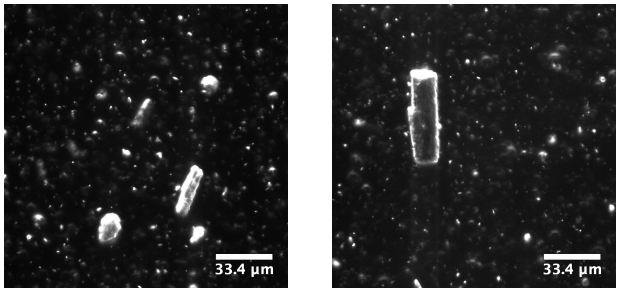

(d) c=4 mg/ml **(e)** c=5 mg/ml

Figure 4.3: Dark field images of toulene mediated dye-doped PDMS

Even though acetone has a closer solubility parameter (δ=9.9 $cal^{1/2}cm^{-3/2}$) to PDMS (δ=7.3 $cal^{1/2}cm^{-3/2}$) than acetonitrile (δ=11.9 $cal^{1/2}cm^{-3/2}$)[69], it is found that using acetone as the solvent to dissolve the dye molecule before cooperated with PDMS will lead to even more aggregation of dye molecule than using acetonitrile. Therefore, acetone is not considered to be an ideal solvent incorporated with dye molecule and PDMS.

The absorptivity of the dye-doped PDMS layer using acetonitrile as the solvent is measured and ploted in figure 4.4. The thickness of the sample is measured to be 21.5 μm. With the increase of dye concentration from 1 to 20 mg/ml, the absorptivity at 1064 nm raises up from 4.96 to 28.59 mm^{-1}. Whereas the minimum absorptivity can always be found at around 590 nm, the maximum value appear at around 1064 nm except for c=15 and 20 mg/ml, which exhibit the bathochromic shift of the highest peak and the absence of the turning band at around 500 nm. The position of the maximum and minimum absorptivity conform with the spectrum in figure 4.1 obtained from the solvent, however, the originated highest absorption peak is broaden resulting in a wide absorptive band typically range from 800 to 1600 nm. As it is discussed previously, absorptivity would get saturated at relatively high dye concentrations, i.e. c = 15 to 20 mg/ml. One can predict that the spectrum of absorptivity with even a higher concentration than 20 mg/ml will more or less overlap with the present one.

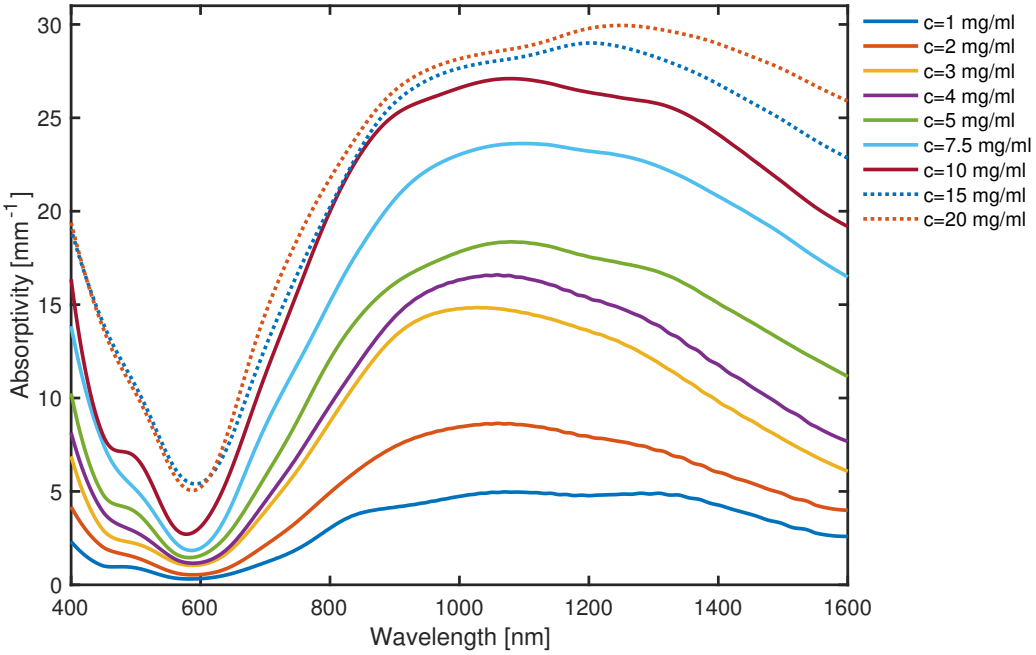

Figure 4.4: Plot of the absorptivity of dye-doped PDMS mediated by acetonitrile with dye concentration from 1 to 20 mg/ml.

The homogeneity of the heat source density depends strongly on the conditions of dye molecules distribution in the cured PDMS matrix. Figure 4.5 shows the dark field images of 21.5 μm thick PDMS chips loaded with varying concentrations of NIR dye molecules using acetonitrile as a transferred mediator.

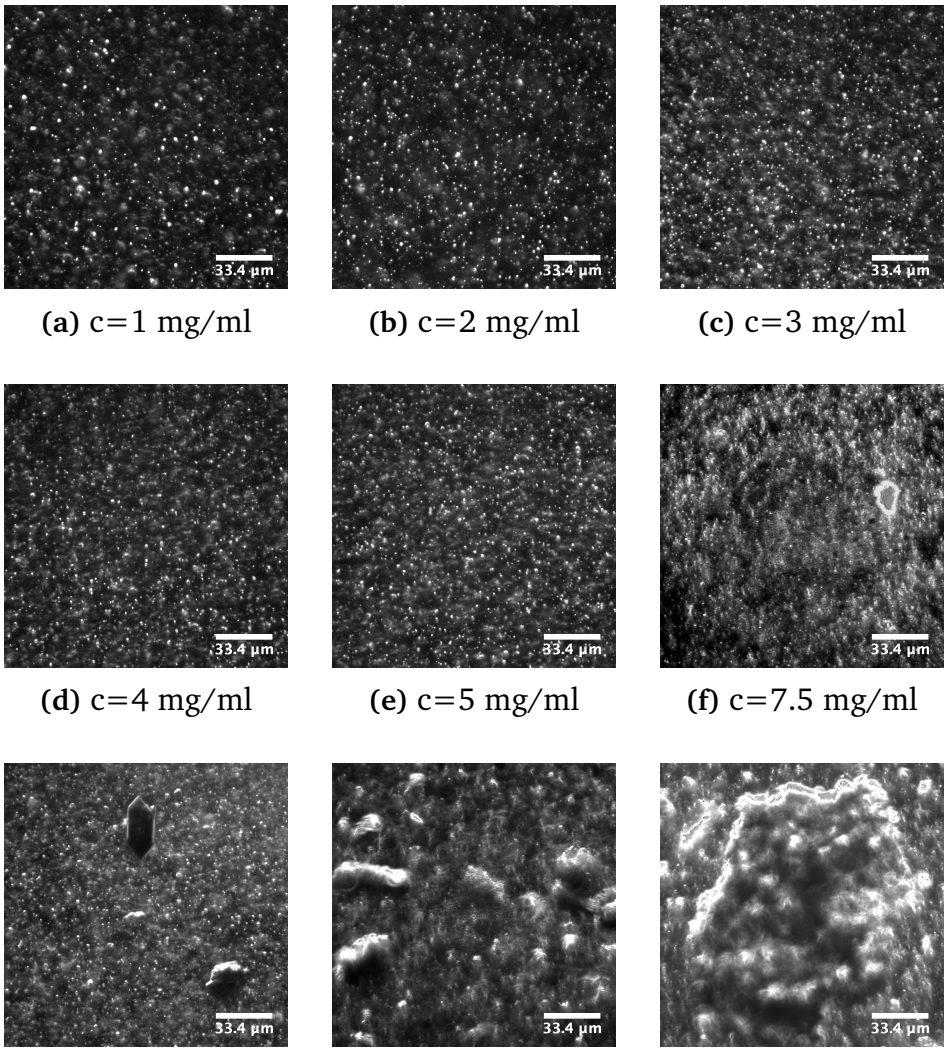

(a) c=1 mg/ml **(b)** c=2 mg/ml **(c)** c=3 mg/ml

(d) c=4 mg/ml **(e)** c=5 mg/ml **(f)** c=7.5 mg/ml

(g) c=10 mg/ml **(h)** c=15 mg/ml **(i)** c=20 mg/ml

Figure 4.5: Dark field images of acetonitrile mediated dye-doped PDMS. Scale bar is equal to 33.4 μm.

As the dye concentration increased from 1 to 5 mg/ml (a-e), dye molecules remain well distributed and can be identified as discrete white dots across the field of vision. However, dye molecules start to form isolated huge crystals in diverse shapes at dye concentration above 7.5 mg/ml (f-i), and the diameters of these crystals (above 10 μm) tend to grow with the concentration. Particularly, in the case of the highest concentration i.g. c=15, 20 mg/ml (h,i), the system completely lost its uniformity and the molecules form into large aggregations. In fact, the dye concentration increase from 15 to 20 mg/ml does not lead to a significant increase in the absorption. As the corresponding absorptivity plot shown in figure 4.4 (indicated by red and blue dashed line), one can possibly anticipate that the random aggregations cause the deformation of the absorption spectrum. Therefore, a reasonable concentration which can provide an approximate homogeneous media should be restricted under 5 mg/ml to avoid significant molecule aggregations. Indeed, acetonitrile is a relatively satisfactory transfer solvent to enhance

the homogeneity of the NIR dye molecules distribution in the PDMS matrix, and it is the only solvent that has been used in the rest of the studies.

To further show how the absorptivity change with the dye concentration in a specific wavelengths, the absorptivity of dye-doped PDMS at 532 and 632 nm follow the linear relation with a dye concentration range from 0 to 20 mg/ml and the fitting are shown in figure 4.6 indicated by green and red dasheded lines, respectively. Simultaneously, as the absorptivity at 1064 nm grows much slower in high concentration and tend to regress above 20 mg/ml, a logarithmic curve fitting (black dashed line) is applied on the measured data (black open circle) of absorptivity at 1064 nm versus dye concentration. The reason for analyzing the absorptivity at 532, 632, and 1064 nm here is to indicate the potential application at three commonly used laser emission wavelength.

In order to quantify the difference of absorption in the visible light and NIR region, the plots in figure 4.7 show the absorptivity ratio between 1064 nm and 532/633 nm altered by the dye concentration. The absorptivity ratio, both 1064 nm/ 532 nm and 1064 nm/633 nm largely decrease as the dye concentration is higher than 5 mg/ml, implying that when the PDMS layer is doped with high concentrations of dye molecules, the absorption in the visible wavelength will become significant, even though a higher absorption can be obtained at 1064 nm thereby reducing the ratio of the NIR to the visible absorption. This should be considered if multichromatic irradiation is simultaneously operated and selective absorption is desired only in the NIR, e.g., when 1064 nm (Nd:YAG) laser is used for light-heat conversion while mercury lamp (546 nm) is used for fluorescence illumination.

In conclusion, to balance the sufficient NIR absorption and the probability of dye aggregation formation that will change the absorption spectrum, the optimized dye concentration in the PDMS matrix is 5 mg/ml.

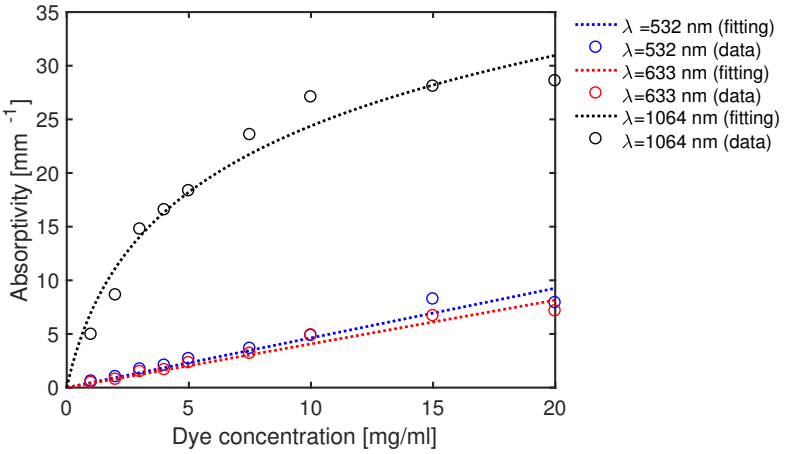

Figure 4.6: Plot (open circle) and fitting (dashed line) of absorptivity of dye-doped PDMS at 532 (green), 632 (red) and 1064 nm (black) versus dye concentration range from 0 to 20 mg/ml.

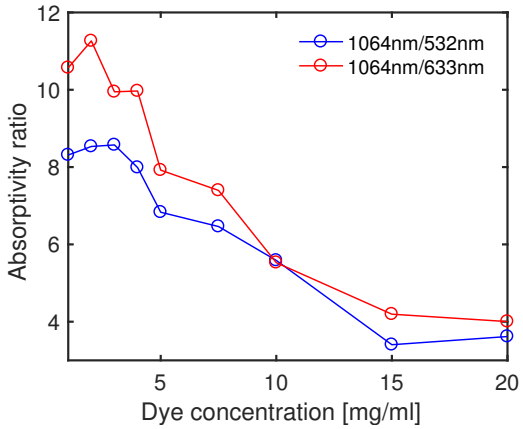

Figure 4.7: Absorptivity ratio of 1064 nm/532 nm (red line and circle) and 1064nm/633nm (blue line and circle) versus dye concentration range from 0 to 20 mg/ml.

4.2 Absorption and Thermal Optimization in Design and Fabrication of NIR-absorbing Agent

Since the absorption spectrum of the NIR-absorber at different concentrations has been obtained from the last section, it can then be used to simulate how will the system absorption change with absorber thickness using transfer matrix method. Beyond the optical simulation, COMSOL multiphysics is employed to simulate the thermal performance of heat generation system determining the relation among the physical configuration, laser power, and temperature increase.

4.2.1 Transfer Matrix Method

In order to investigate the relation between absorption of the NIR-absorber and the absorbing layer thickness, the transfer matrix method is carried out to calculate the propagation of the light within dye-doped PDMS films. Figure 4.8 shows that the simulated absorption at 532 (blue line), 632 (green line) and 1064 nm (red line) as the absorber thickness ranged from 0 to 100 μm under the dye concentration c=5 mg/ml. Approximately 38%, 11% and 8% absorption at 1064, 532 and 632 nm, respectively, can be obtained when the thickness reaches 20 μm , and in an extreme case a 100 μm absorber is able to offer more than 80% absorption at 1064 nm, 45% at 532 nm and 36% at 632 nm.

Furthermore, by changing the concentration from 0.5 to 10 mg/ml, we can explore the relation between absorption and thickness under each concentration, as demonstrated in figure 4.9. The growth of absorption over thickness can be regarded as a linear trend at 532 (a) and 632 nm (b), and the absorption significant enhance as the concentration increase. A linear to quadratic thickness dependency is observed between absorption at 1064 nm and absorber thickness as the concentration increased from 0.5 to 10 mg/ml (figure 4.9 c).

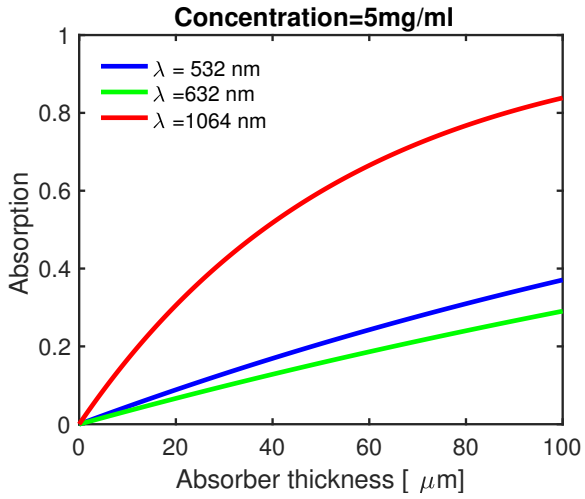

Figure 4.8: Absorption of absorber layer with increasing thickness at 532nm (blue line), 632nm (green line) and 1064nm (red line). dye concentration c=5 mg/ml.

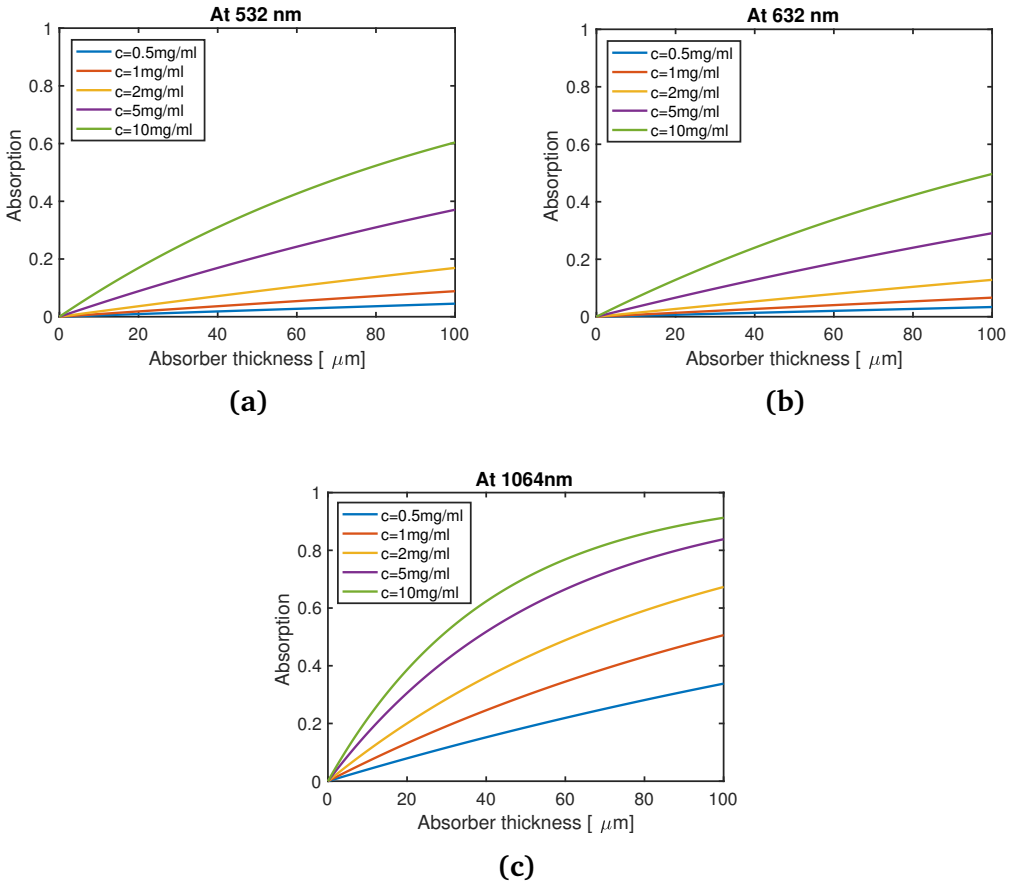

Figure 4.9: Absorption of absorber layer with dye concentration equal to 0.5 (blue line), 1 (orange line), 2 (yellow line), 5 (purple line) and 10 mg/ml (green line) as thickness increased from 0 to 100 um at 532 (a), 632 (b) and 1064 nm (c).

Based on the fabrication of NIR-absorbing PDMS thin film mentioned in section 3.2, the obtained thickness can be tuned from 15 to 100 μm. Therefore, to

avoid the significant absorption in the visible wavelength and achieve adequate NIR absorption, through transfer matrix method the optimized absorber thickness is assigned to be 20 μm providing more than 30% of absorption at 1064nm.

4.2.2 COMSOL Multiphysics Thermal Simulation

To evaluate the local temperature increase on the surface of the NIR absorbed system in the aqueous solution environment, COMSOL multiphysics is applied to simulate the heat transfer. The absorption measured from UV-vis spectroscopy is the optical property of the bulk materials with the assumption of uniform dye molecule distribution in the PDMS matrix. However, it is clear to see the aggregations of dye molecule in the darkfield image (figure 4.5), revealing the significant inhomogeneity in the heat source. In addition, the molecule scattering will be measured as the absorption in the UV-vis spectroscopy measurement, which contributes to the overestimation of the absorption in the dye-doped PDMS layer. Therefore, in COMSOL simulation, the absorption efficiency is scaled to be one third of the calculated value from the transfer matrix method.

Figure 4.10 visualizes the temperature increment on the x-y plane, where x-axis is the radial distance on the surface of PDMS away from the heat source up to 20 μm, indicated as a dashed arrow in figure 3.2, and y-axis is the applied NIR laser power ranged from 0 to 150 mW in the case without (figure 4.10a) and with (figure 4.10b) the spin-on glass on top of the PDMS layer. The simulated thickness of PDMS and spin-on glass are 20 μm and 1 μm, respectively. The temperature in the boundary between gray and blue area in the figure indicates the gel-to-liquid phase transition temperature of DSPC lipids (55°C), and the combinations of radial distance and laser power situated in the multicolored region favors the phase transition of the lipid. It is predicted that the minimum powers used to trigger the phase transition process are approximately 16 mW and 29 mW in terms of the absence and presence of spin-on glass, respectively. Additionally, the highest temperature generated by the maximum laser power with the spin-on glass can even reach above 570°C (figure 4.10a), which surpasses the decomposition temperature of PDMS ($\approx$460°C) and the typical organic molecules[70], and thus the heating agent containing dye-doped PDMS could highly undergo thermal degradation. This could also lead to the irreversible damage of the lipid molecules deposited on top, threatening their diffusive property[71]. Therefore, applying spin-on glass on top of the NIR absorber seems to be an appropriate alternative in our case. In the following section, the corresponding experiment is carried out to verify the heat transfer in simulation.

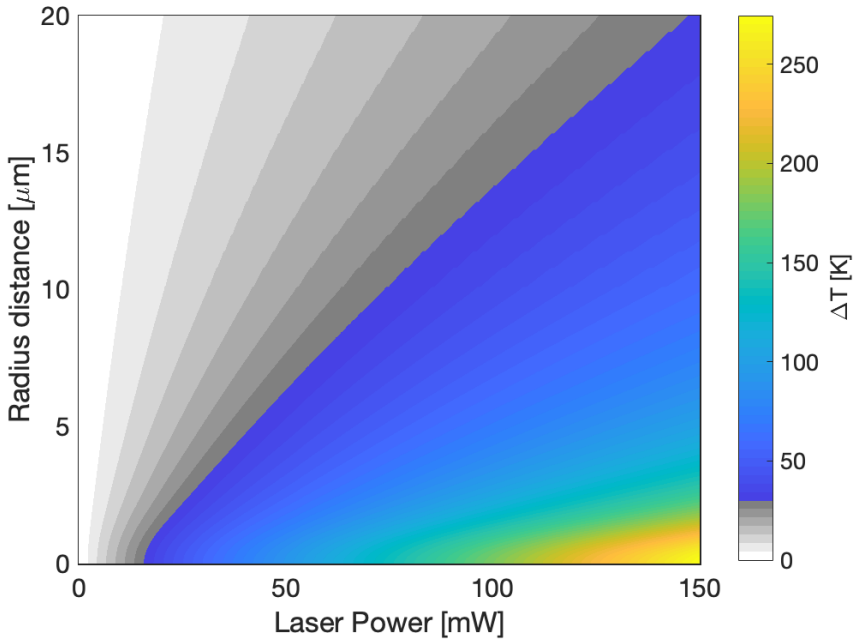

(a)

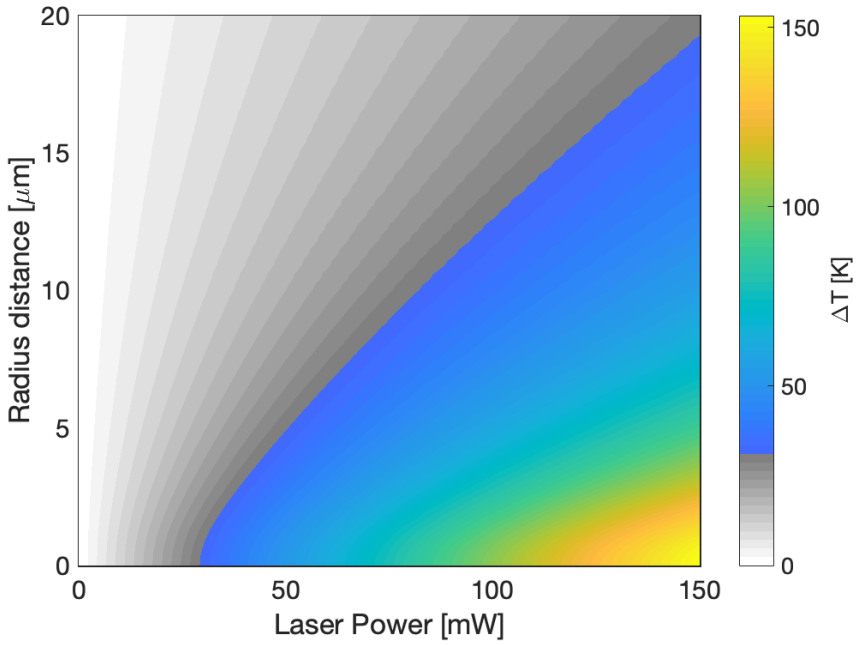

(b)

Figure 4.10: Color plot showing the simulated temperature increase over radial distance when using 0-150 mW NIR laser power. Δ T=T-T_0 and T_0 is the room temperature 293.15 K. (a) on the surface of dye-doped PDMS; (b) on the surface of spin-on glass.

4.3 Thermodynamic Response of Lipid Vesicles and Bilayers

In this section, regarding the versatile properties of lipid molecules, two cases of attractive study on lipids are introduced. The first study utilizing POPC lipid to explore the supported lipid-bilayers formation promoted by local heating, followed by the FRAP experiment to determine the lateral mobility of the SLBs. The second study is using DSPC lipid to investigate their phase transition and a serious of derived experiment including analogue FRAP in gel phase lipid and gel phase lipid lithography. All the lipid materials are labeled with fluorophores, which has the absortion peak at around 530 to 570 nm[72]. This matches the emission wavelength of mercury lamp and the green laser, and therefore lipid vesicle and bilayers can be observed under fluorescent microscopy.

4.3.1 Study 1: Fluidic Phase POPC Phospholipid

POPC lipid is one of the most common used fluidic phase lipid materials at room temperature, and it exhibits advantage in forming supported lipid-bilayers. In this study, two experiments are carried out using POPC lipid: investigating SLBs formation in the presence of thermal environment, and determing the lateral mobility of POPC lipid on a silicon-based polymer substrate by FRAP experiment.

4.3.1.1 Promoted Supported Lipid-bilayers Formation

The formation of support lipids bilayers (SLBs) in fluidic phase can only be triggered when surface fused vesicles reach a critical vesicle coverage, which is associated with the initial vesicles concentration in solution. However, it can be highly promoted by local heating induced by a 60 mW NIR laser on a oxidized PDMS (ox-PDMS), as shown in (a)-(c) in figure 4.11. The thickness of the PDMS layer is 22 μm. Prior to the exposure of the NIR laser (a), the fluorescent labeled vesicles that attached on the PDMS surface can be observed as white dots distributed across the field of vision. Note that the small areas of SLBs can be seen near the top and left corner. Once the laser emission initiates (b), a circular region with around 30 μm radial get blurred, and its central intensity decreases dramatically. After 2 s of NIR laser irradiation, the intensity of the blurred area immediately recovers and the homogeneity remains, indicating that the lipid-bilayers have been established within this circular area and even merged with the already existing SLBs. Even though the mechanism of such unusual SLBs formation have not been completely understood, one can suggest that the change of surface tension induced by heat generation contributes to a higher lateral diffusion coefficient of POPC lipids, promoting extra ruptures of the adhered vesicles. As a result, such vesicles tend to fuse with each other forming lipid-bilayers.

As a control experiment, a pure PDMS without any dye molecules is used in the same configuration. Following the same procedure, no comparable effect can be seen (figure 4.11d-f). It is known that the absorption coefficient of PDMS material and liquid water are 2.86 and 0.15 cm^{-1}[32, 73], respectively, which are much

lower than the absorption coefficient of dye-doped PDMS (α = 160 cm^{-1}). These two sets of experiments successfully verify the ability for NIR-dye-based absorbing system to accomplish a light-to-heat conversion, although the heat generation has not been quantified yet.

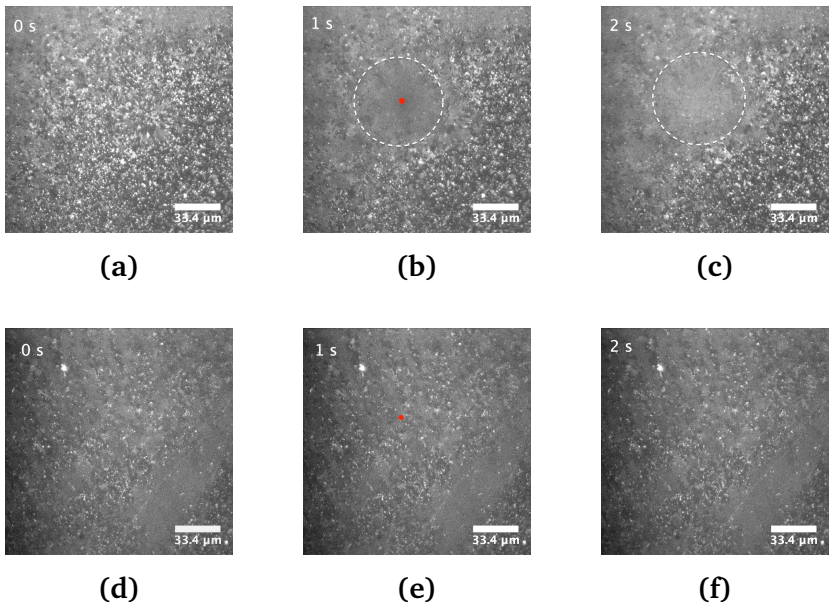

Figure 4.11: Fluorescent images of support lipid-bilayers formation promoted by NIR laser (60 mW) irradiation (indicated by red dot) on ox-PDMS dye-doped(a-c) and pure PDMS(d-f). (a) and (d) Before the NIR laser is on (0s), the unhomogeneous area represent attached vesicles on PDMS. (b) and (e) NIR laser is on for 1s. (c) After illuminated by NIR laser for 2s, the exposured region gain higer homogeneity intensity since support lipid-bilayers were formed indicated as dashed line, whereas no SLBs were formed in (f).

4.3.1.2 FRAP Measurements of POPC Lipid-bilayers on the Surface of Ox-PDMS

FRAP is applied to inspect the lateral mobility of POPC lipids bilayer on ox-PDMS. The individual fluorophore in the lipid membranes is exposed to an intense 532 nm laser light and undergoes a photodegradation, resulted from the inter-system crossing from the singlet state to the triplet state, and therefore it is unable to fluoresce[74]. However, the lateral mobility of the lipid-bilayers allow the bleached and unbleached lipids to diffuse and promote the recovery of fluorescence intensity within the bleached spot. Figure 4.12 shows the recovery curve from the FRAP data revealing the raise of the fluorescence intensity with the time. Sim-FRAP, a plugin in ImageJ, has been used to correlate the recovery curve based on the FRAP images. The lateral diffusion coefficient of POPC lipid-bilayers is subsequently calculated as 1.24 μm^{2}s^{-1}. This is comparable with the diffusion coefficient of POPC lipid on the glass substrate (D=1.0 $\pm$ 0.2 μm^{2}s^{-1} [75]), which is also hydrophilic like the ox-PDMS. Therefore, we believe lipid-bilayers were obtained rather than lipid monolayers. In fact, lipid-bilayers always exhibit higher lateral mobility than

a monolayer, which lacks an ultra-thin lubricated liquid layer, existing between the phospholipid headgroups and the support substrate[76]. It is argued that the diffusion coefficient of the lipid-bilayers is determined by the applied analytical method for the FRAP experiment[77, 78]. And the addition of polyethylene glycol in the phospholipid can in principle alter its diffusivity since the polymer can extend the lubricating water layer even though the precise understanding of such mechanism is still absent.

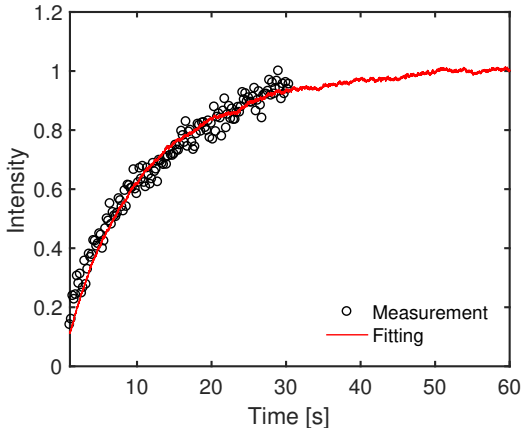

Figure 4.12: Plot of the recovery curve in FRAP experiment in terms of POPC SLBs formed on ox-PDMS. Diffusion coefficient D is determined to be 1.24 $\mu m^2 s^{-1}$

4.3.2 Study 2: Thermodynamic Response and Thermal Manipulation of DSPC Phospholipid

In contrast to POPC, DSPC lipid exists as a gel phase at room temperature which makes it become an ideal object for studying the phase behavior in a well-controlled way. This study can be divided into three parts, started by the exploration of how the heating laser power can influence the phase transition. The second part contains the analogue FRAP experiment in DSPC to further investigate its phase transition behaviour. Finally, derived from this, a concept called gel phase lipid lithography is established and displays impressive thermal characteristic of the DSPC lipid.

4.3.2.1 Phase Transition of DSPC Phospholipid

In order to further visualize the thermal effect created by the absorption of NIR dye, DSPC lipid, which has the gel-to-fluidic phase transition temperature at 55^oC, is employed here as a probe of temperature distribution. By labeling a small fraction of DSPC lipid with a fluorophore, the process of phase transition can be precisely monitored. Figure 4.13 displays the phase transition of DSPC lipids when the local heating is on in a time period of 4 seconds. In the initial state (a), the labeled vesicles (indicated as the brightest area) are absorbed and isolated on the surface. Once the NIR-laser is operated (b), the heated region rapidly turns into a circular pattern, and the diameter of such round-shape arena grows over

time (b)-(e), and arrives a stable value in 4 seconds of exposure time (f). Within the ring area in figure 4.13 f, the fractured pattern disappears and is replaced by a continuous region with intermediate intensity. This is due to the fact that the corresponding local temperature increases above the transition temperature of DSPC lipids so that they can exist in fluidic phase and thus gain their lateral mobility, which facilitates the vesicles to diffuse and rupture and eventually form the SLBs across the phase transition area. It is noted that the fluorescence intensity in the interior of this ring pattern (the hole of the doughnut), where the highest temperature is, get highly reduced, A possible explanation could be the negative dependence of the fluorescence intensity of rhodamine B, contained in the label lipids, on temperature[79], and the high temperature could lead to the photochemical/thermal degradation of the lipid molecules.

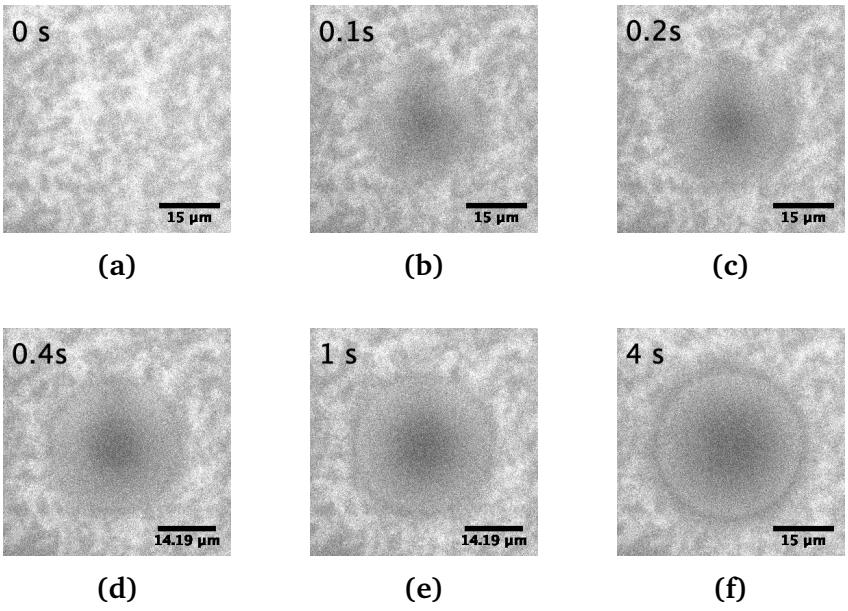

Figure 4.13: Fluorescent images of DSPC lipid phase transition triggered by a 120 mW 1064 nm laser for 4 s on ox-PDMS. (a) Pre-exposure to NIR laser. Labeled and unlabeled vesicles are indicated as white and grey area. (b) Phase transition area appear at 0.1s after NIR laser emission. (c)-(f) Phase transition region grow over exposure time.

For heat generation applications, it is important to correlate the temperature distribution with the heating laser power, which has been numerically simulated in COMSOL in section 4.2.2. This can also be realized in the experiment that by varying the laser power, the phase transition area presents with corresponded diameter, shown in figure 4.14. The lipid vesicles used in this study are all labeled in order to obtain a strong fluorescence signal and a clear borderline between the gel phase and liquid phase lipid region. This study is carried out on the surface of 1 μm thick spin-on glass above dye-doped PDMS, and its advantage is to provide a high compatibility substrate for lipid vesicles to form SLB in a better condition compared to the PDMS, which is a porous material. Under relatively low laser power (a)-(b), insufficient heat has been generated, and thus the phase transi-

tion is absent. As it is expected, the measured diameter of phase transition area efficiently expand as the applied laser power is increased, resulting in approximately 4.5, 16.7, 22.54, 32.06 μm in diameter when laser power is 24, 36, 60 and 120 mW, respectively. However, this demonstrates a more effective heating from the experiment compared to the thermal simulation (figure 4.10), which requires more than 35 mW laser power to initiate the phase transition and with 120 mW laser power it can only develop a phase transition region with diameter less than 12 μm. The measured radial in each image in figure 4.14 are plotted in the coordinate of the radial distance and the laser power, indicated as the red squares in figure 4.15.

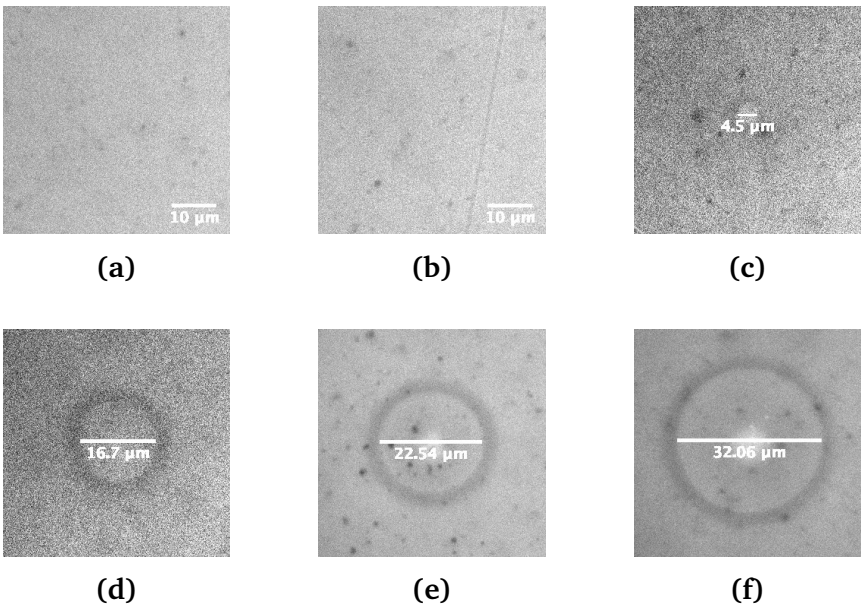

Figure 4.14: Fluorescent images of DSPC lipid transition on 1 μm thick spin-on glass above the dye-doped PDMS. The applied 1064 nm laser powers are 6 (a), 12 (b), 24 (c), 36 (d), 60 (e) and 120 mW (f). Scale bars in (c)-(f) indicate the diameter of the phase transition region.

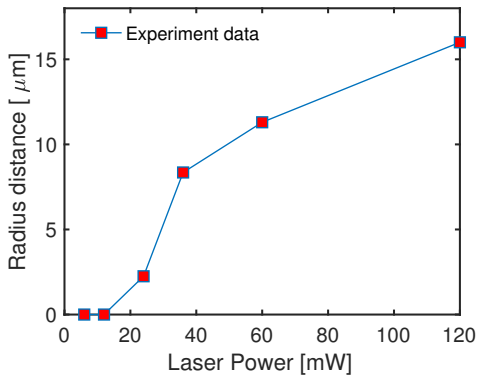

Figure 4.15: Plot of radial distance along with NIR laser power obtained from experiment.

Apparently, the radius of the phase transition region raises non-linearly with the laser power, and the temperature increase is more efficient in reality than in the simulation. Several factors could contribute to such variation, and one of them could be the inhomogeneity of the heat source density originated from the non-uniform distribution of the dye molecules in the polymer matrix, which has been revealed in darkfield image in section 4.1. Another reason could be the thickness deviation of the spin-on glass as the temperature dissipation which highly depends on the distance away from the heating spot. Also, focus condition of the laser beam can influence the volume of the heat source and thus lead to this divergence.

4.3.2.2 Analogue FRAP in DSPC Phospholipid

Taking the advantage of DSPC with a transition temperature above room temperature, one can further investigate the diffusion of DSPC lipid at elevated temperatures. Figure 4.16 indicates the process of the fluorescence photobleaching recovery activated by local heating on spin-on glass. The field of vision is filled with the absorbed label DSPC vesicles (a), and local heating is generated establishing a phase transition circular area after exposure to a 60 mW 1064 nm laser for 10 s (b). By focusing a 532 nm green laser in the center of this ring-like pattern for 10 s, a bleached spot on the order of a few micrometers is obtained (c). In the case that all the lipids are in gel phase once the NIR laser is off, the bleached lipids are not able to diffuse around and will be endlessly trapped in the same position. The bleached area completely recovers after the exposure of 1064 nm laser (d), which enables the lipid within the heated region to transition from gel phase to fluidic phase again, thereby permitting lateral diffusion. It is interesting that the NIR laser plays a role of a trigger to release lipid diffusion within the restricted area. One assumption has also been proven that the "negative label" lipids, i.e. the bleached lipids, have the ability to move around in the whole ring pattern and switch with the other lipids, implying that such a ring pattern should be regarded as lipid-bilayers with a two-dimensional fluidity.

A comparable experiment is carried out demonstrating the entire photobleaching induced by the local heating on spin-on glass, as shown in figure 4.17. The first step of the process is similar to the previous study, i.e. a 1064 nm laser is focused on the spin-on glass attached with vesicles for 10 s forming a circular pattern (a)-(b). The sample is then exposed to a 1.25 mW 532 nm laser and a 60 mW 1064 nm laser simultaneously for 25 s, ultimately leading to the complete photobleaching within the circular pattern (e). Note that the fluorescence signal gradually diminishes over exposure time as it can be seen in (c)-(d) when the mercury lamp illumination is removed. Since the gel phase lipids in the outside of this fluidic region are not capable of diffusing in and served as supplyments, as the green and NIR laser are simultaneously operated, each lipid in fluidic phase would be bleached out once they diffuse across the 532 laser beam, and finally, all the lipids lost their fluorescence intensity. However, it is odd that the interior of the circular area exhibits a quantitatively higher fluorescence, surrounded by a much darker annulus compared with the ambient area in the field of vision (b to d).

Two different analogue FRAP experiments in DSPC lipid successfully prove the

photothermally controlled lateral diffusion in the lipid phase transition. This NIR laser induced process thus becomes the fundamental of the thermal manipulation of the gel phase lipid, which will be introduced in the next section.

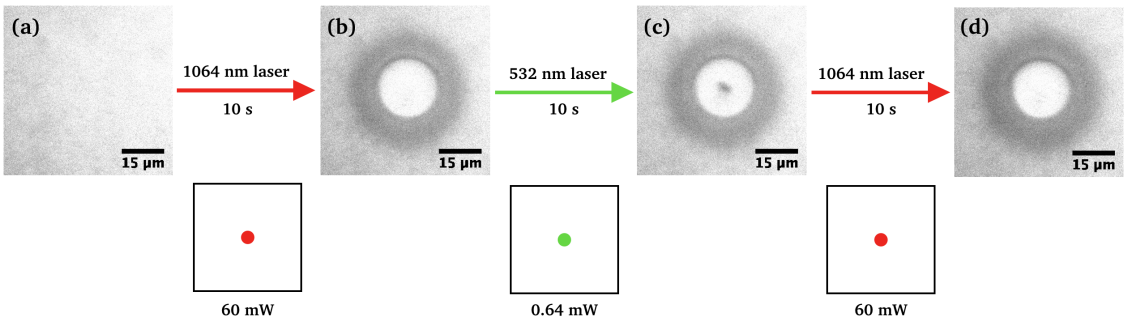

Figure 4.16: Fluorescence images of fluorescent bleaching recovery by local heating. Label DSPC vesicles absorbed on spin-on glass exhibit a uniform fluorescence signal across the field of vision (a). After irradiated by a 60 mW 1064 nm laser for 10 s, a ring shape phase transition region appears (b). A 532 nm laser is focused in the center of the ring pattern for 10 s creating a dark bleached dot (c). The sample is irradiated again by a 60 mW 1064 nm laser eventually resulting in a recovery of the bleached area.

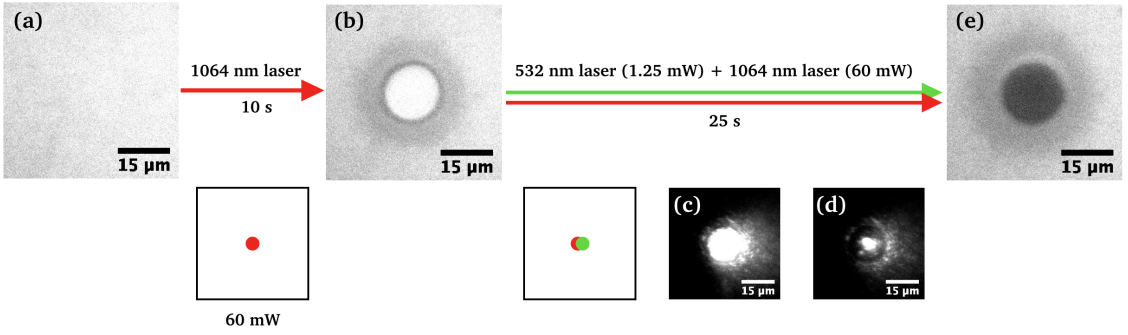

Figure 4.17: Fluorescence images of entire fluorescent bleaching induced by local heating. Label DSPC vesicles absorbed on spin-on glass exhibit a uniform fluorescence signal across the field of vision (a). After irradiated by a 60 mW 1064 nm laser for 10 s, a ring shape phase transition region appears (b). A 532 nm laser and a 1064 nm laser are simultaneously focused at the center of the ring pattern for 25 s, causing entire photobleaching within the ring pattern (e). (c) and (d) show the process of photobleaching without mercury lamp illumination.

4.3.2.3 Gel Phase Lipid Lithography

When the focal plane of the laser beam is moved away from the interface between the spin-on glass and the buffer solution, i.e. the laser beam is out of focus, the beam width in the heat source will expand and thus the heated area will highly increase. This can be used to create a larger phase transition allowed area since the more gentle temperature gradient is generated.

In figure 4.18, a series of fluorescence images introduce the process of gel phase lipid lithography by using a green and NIR laser. To initiate, labeled DSPC phospholipid vesicles are deposited on the surface of spin-on glass at room temperature. Since the excitation wavelength of rhodamine B labeled lipid is in the range of 530-570 nm[72], a 532 nm laser can be used to photobleach the attached lipid vesicles. Gel phase lipids are not allowed to diffuse so that the beam trace is recorded as a pattern of "BNP" by manipulating the sample stage, as shown in figure 4.18 a. A 1064 nm laser is then operated to construct a large scale of phase transition region with the radial around 70 μm, and the bleached letters that are fallen within this circular area have been significantly removed (figure 4.18 b). This is due to the formation of analog lipid-bilayers through the liquid phase adsorbed vesicle rupture and fusion induced by local heating. Once the NIR laser is off, i.e. the lipids transit into gel phase again, a "π" letter is lithographed by using a 532 nm laser with a quantitatively lower contrast to the background, shown in figure 4.18 c. Eventually, the elimination of such new-formed pattern is accomplished by applying NIR laser heating, subsequently leaving a shadow around the center on the field of vision (figure 4.18 d).

In fact, as an extension of FRAP experiment in gel phase lipid, the 532 nm laser and 1064 nm laser function as a writing pen and an eraser in the lipid lithography and it is experimentally proved that a complex design can also be realized assisted by piezoelectrically controlled stage. However, the limitation of such process is that the written contrast will decline in the second time of the green laser lithography (figure 4.18 c). This might be because the fluorescence intensity of the analog lipid-bilayers is quantitatively lower than the small unilamellar lipid vesicles, and as a part of lipid being bleached, the fluorescent density of the transition region consequently declines. The contrast also depends on the writing speed, i.e. the average exposure time on each pixel.

This study show great possibilities on how laser beam can be used as a lithography tool to manipulate the gel phase lipid. This is relied on the optimized heat generation system which is optically transparent and highly absorptive in the NIR regime. Therefore, such system has been proved to have high compatibility on biological samples.

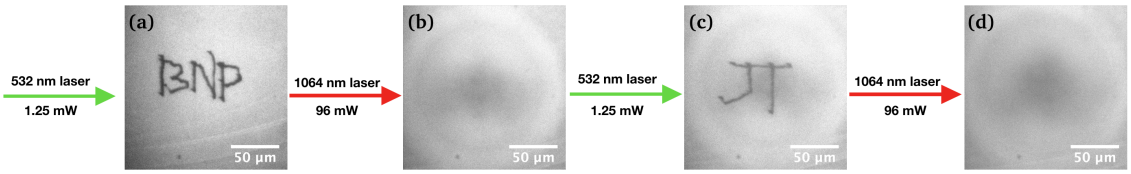

Figure 4.18: Fluorescence images of lipids re-writable lithography from "BNP" to "π". (a) "BNP" is written by 532 nm laser scanning on the DSPC lipids layer, indicated as black traces on the background. (b) The created letters fade away after exposure to the 1064 nm laser. (c) Re-write the "π" by using the 532 nm laser. (d) The written pattern is removed by 1064 nm laser.

5

Conclusion and Outlook

5.1 Summary and Conclusion

In this study, we successively present the local heat generation system utilizing the light-to-heat conversion in micro-scale. Through UV-Vis-NIR spectrophotometer measurements, a specific organic molecule is proved to be an alternative candidate for intensively high absorption in the NIR regime (particularly 1064 nm) apart from the commonly used metal nanoparticles as well as inorganic semiconductors. The bulk material made from such dye molecules exhibits relatively high transmission in the visible wavelength, and due to this selective absorptivity, it is satisfactory to apply to fluorescence detection of the labeled samples. However, it is also found that the increase of dye concentration would induce the massive aggregation of dye molecules, and once it reaches the threshold value (c=10 mg/ml), the maximum absorption peak will shift toward the infrared end. Meanwhile, its absorption gain tends to saturate, and the peak shape gets deformed. These are also signified in the dark field images, which reveal the existence of the conspicuous crystallization of dye particles. The NIR-dye molecules are hosted in the PDMS matrix to construct the NIR-absorber since the PDMS is optically transparent, chemically inert and easy to fabricate.

In order to understand how the system absorption behaves along with the absorbing layer thickness, the transfer matrix method is carried out based on the measured absorptivity of the dye-doped PDMS layer. It is shown that the absorption at 1064 nm with reasonable dye-doped concentration rises non-linearly and reaches 30% in a thickness of 20 μm. One can also obtain more than 80% of absorption with 100 μm absorbing layer, which is potentially capable of infrared light blocking. Apart from the optical simulation, thermal simulation utilizing COMSOL multiphysics gives a prediction of temperature increment of the heat generation system. Illumination with a NIR laser could in principle provide sufficient heating up to few hundreds degree Celsius, and the temperature profile highly depends on the corresponding configuration. By employing a thin layer of spin-on glass on top of the PDMS, the thermal dissipation is much favored giving rise to the considerably smoother temperature gradient across the lateral distance of the sample surface.

Experiments on investigating the thermodynamic response of lipid-bilayers are presented as a significant application of NIR-dye based thermal generation platform. One exciting discovery is that the local heating applied on the surface can facilitate the self-assembly from a liquid crystal phase absorbed vesicle into

corresponding lipid-bilayers. This could be due to the promotion of the vesicles rapture as well as the consequent fusion with higher diffusion freedom. Another impressive exploration utilizing lipid phase transition demonstrates that the photobleached spot within the gel phase lipid can only recover in the assistance of NIR-laser heating reaching above the transition temperature. Meanwhile, derived from this phenomenon we carry out the multi-written gel phase lipid lithography, which functions the visible laser and NIR laser as a pen and an eraser, respectively, to be able to optically print the desired pattern on the canvas made of lipid materials.

5.2 Outlook

As an attempt in the field of NIR photothermal heat generation, the NIR absorbed organic-based material with its unique properties such as relatively high absorption in the NIR as well as being almost transparent in the visible light wavelength, does offer a supplementary alternative beyond plasmonic nanoparticles. Nevertheless, more effort is still needed to optimize such a system in varied manners in order to improve its performance.

It is appreciated to analyze the other type of pigment molecules absorbed in the NIR with even steeper absorption peak centered on 1064 nm. Since the cooperation between the polymer matrix and the dye molecules would profoundly influence their distribution and thus heat source density homogeneity, PDMS can be replaced by the other commonly used media such as SU-8 and PMMA[3]. Moreover, the compatibility among the dye molecules mediated solvent, and polymer matrix shall be carefully examining.

To be able to form a perfect spin-on glass on top of the polymer surface without any cracking, several factors during the fabrication are ought to be investigated to get better control. These include the type of spin-on glass solution, the spin coating speed as well as the time period, the temperature of the hot plate and the final curing time. Furthermore, it is also beneficial to precisely govern the thickness of the glass layer, which can lead to the modification of the generated temperature gradient.

An advanced temperature measurement, as one of the vital topic within the thermodynamics, is highly demanded since the usage of the lipid phase transition as thermometry were not sufficiently reliable in the micro-scale region. A possible solution is to employ either fluorescence lifetime of the specific fluorophore or the coil to globule transition of a lower critical solution temperature polymer in the solution[80, 7]. Apart from the thermal encouraged vesicle self-assembly and the phase transition of lipid films, there are many potential options using this home-made photothermal system to study their thermodynamic response . One ideal candidate could be to explore the thermophoresis of the lipid membrane-embedded compounds. In detail, the NIR laser is redirected by a spatial light modulator (SLM), which imposes a designed form of spatially-varying modulation on a laser beam[13]. Such processed laser beams are focused on the absorbing layer establishing a versatile temperature gradient, and by varying the exposure area as the pre-determined pattern, one can thermophoretically manipulate the

integrated component on the membrane such as protein and cholesterol-tagged DNA[10, 81]. Such setup is able to realize the dynamic trapping as well as concentrating of thermophobic motion particles when a doughnut shapes laser beam is applied and continuously shrinking in its radius, as illustrated in figure 5.1.

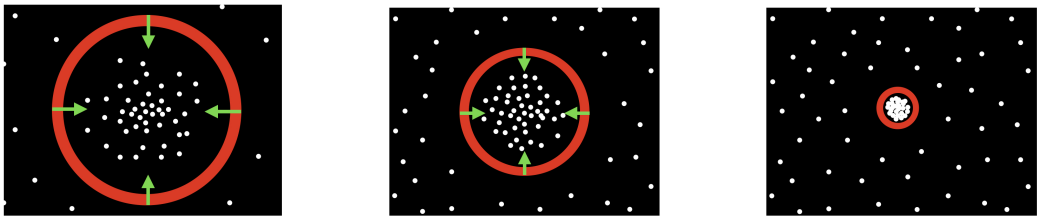

Figure 5.1: Illustrations of temperature gradient confinement of lipid membrane embedded compounds (top view). White dots denote the fluorescent labeled components tethered on the SLB and red ring-patterns denote the NIR-laser exposure region. The green arrows indicate the migration direction of the these compounds.

Bibliography

[1] Moran Jerabek-Willemsen, Chistoph J Wienken, Dieter Braun, Philipp Baaske, and Stefan Duhr. Molecular interaction studies using microscale thermophoresis. *Assay and drug development technologies*, 9(4):342–353, 2011.

[2] Chao Zhao, Alparslan Oztekin, and Xuanhong Cheng. Measuring the thermal diffusion coefficients of artificial and biological particles in a microfluidic chip. In *APS Division of Fluid Dynamics Meeting Abstracts*, 2013.

[3] Lasse H Thamdrup, Niels B Larsen, and Anders Kristensen. Light-induced local heating for thermophoretic manipulation of dna in polymer micro-and nanochannels. *Nano letters*, 10(3):826–832, 2010.

[4] Stefan Duhr and Dieter Braun. Why molecules move along a temperature gradient. *Proceedings of the National Academy of Sciences*, 103(52):19678–19682, 2006.

[5] Christoph J Wienken, Philipp Baaske, Stefan Duhr, and Dieter Braun. Thermophoretic melting curves quantify the conformation and stability of rna and dna. *Nucleic acids research*, 39(8):e52–e52, 2011.

[6] Philipp Reineck, Christoph J Wienken, and Dieter Braun. Thermophoresis of single stranded dna. *Electrophoresis*, 31(2):279–286, 2010.

[7] Irep Gözen, Mehrnaz Shaali, Alar Ainla, Bahanur Örtmen, Inga Poldsalu, Kiryl Kustanovich, Gavin DM Jeffries, Zoran Konkoli, Paul Dommersnes, and Aldo Jesorka. Thermal migration of molecular lipid films as a contactless fabrication strategy for lipid nanotube networks. *Lab on a Chip*, 13(19):3822–3826, 2013.

[8] Emma L Talbot, Jurij Kotar, Lucia Parolini, Lorenzo Di Michele, and Pietro Cicuta. Thermophoretic migration of vesicles depends on mean temperature and head group chemistry. *Nature communications*, 8:15351, 2017.

[9] Emma L Talbot, Lucia Parolini, Jurij Kotar, Lorenzo Di Michele, and Pietro Cicuta. Thermal-driven domain and cargo transport in lipid membranes. *Proceedings of the National Academy of Sciences*, 114(5):846–851, 2017.

[10] Eric H Hill, Jingang Li, Linhan Lin, Yaoran Liu, and Yuebing Zheng. Optothermophoretic attraction, trapping, and dynamic manipulation of lipid vesicles. *Langmuir*, 34(44):13252–13262, 2018.

[11] Christoph J Wienken, Philipp Baaske, Ulrich Rothbauer, Dieter Braun, and Stefan Duhr. Protein-binding assays in biological liquids using microscale thermophoresis. *Nature communications*, 1:100, 2010.

[12] Susanne AI Seidel, Christoph J Wienken, Sandra Geissler, Moran Jerabek-Willemsen, Stefan Duhr, Alwin Reiter, Dirk Trauner, Dieter Braun, and

Philipp Baaske. Label-free microscale thermophoresis discriminates sites and affinity of protein–ligand binding. *Angewandte Chemie International Edition*, 51(42):10656–10659, 2012.

[13] Linhan Lin, Xiaolei Peng, Xiaoling Wei, Zhangming Mao, Chong Xie, and Yuebing Zheng. Thermophoretic tweezers for low-power and versatile manipulation of biological cells. *ACS nano*, 11(3):3147–3154, 2017.

[14] Chen-Yuan Wang, TF Morse, and JW Cipolla. Laser-induced natural convection and thermophoresis. *Journal of heat transfer*, 107(1):161–167, 1985.

[15] Ross T Schermer, Colin C Olson, J Patrick Coleman, and Frank Bucholtz. Laser-induced thermophoresis of individual particles in a viscous liquid. *Optics express*, 19(11):10571–10586, 2011.

[16] Andrew M Smith, Michael C Mancini, and Shuming Nie. Bioimaging: second window for in vivo imaging. *Nature nanotechnology*, 4(11):710, 2009.

[17] Liselotte Jauffred, Akbar Samadi, Henrik Klingberg, Poul Martin Bendix, and Lene B Oddershede. Plasmonic heating of nanostructures. *Chemical reviews*, 119(13):8087–8130, 2019.

[18] J Eichler, J Knof, and H Lenz. Measurements on the depth of penetration of light (0.35–1.0 μm) in tissue. *Radiation and environmental biophysics*, 14(3):239–242, 1977.

[19] Eva Hemmer, Antonio Benayas, François Légaré, and Fiorenzo Vetrone. Exploiting the biological windows: current perspectives on fluorescent bioprobes emitting above 1000 nm. *Nanoscale Horizons*, 1(3):168–184, 2016.

[20] Susanne AI Seidel, Niklas A Markwardt, Simon A Lanzmich, and Dieter Braun. Thermophoresis in nanoliter droplets to quantify aptamer binding. *Angewandte Chemie International Edition*, 53(30):7948–7951, 2014.

[21] Karina Zillner, Moran Jerabek-Willemsen, Stefan Duhr, Dieter Braun, Gernot Längst, and Philipp Baaske. Microscale thermophoresis as a sensitive method to quantify protein: nucleic acid interactions in solution. In *Functional Genomics*, pages 241–252. Springer, 2012.

[22] Dieter Braun and Albert Libchaber. Trapping of dna by thermophoretic depletion and convection. *Physical review letters*, 89(18):188103, 2002.

[23] Jon S Donner, Guillaume Baffou, David McCloskey, and Romain Quidant. Plasmon-assisted optofluidics. *Acs nano*, 5(7):5457–5462, 2011.

[24] Steven Jones, Daniel Andren, Pawel Karpinski, and Mikael Kall. Photothermal heating of plasmonic nanoantennas: influence on trapped particle dynamics and colloid distribution. *ACS Photonics*, 5(7):2878–2887, 2018.

[25] Kohei Mizuno, Juntaro Ishii, Hideo Kishida, Yuhei Hayamizu, Satoshi Yasuda, Don N Futaba, Motoo Yumura, and Kenji Hata. A black body absorber from vertically aligned single-walled carbon nanotubes. *Proceedings of the National Academy of Sciences*, 106(15):6044–6047, 2009.

[26] EA Taft and HR Philipp. Optical properties of graphite. *Physical Review*, 138(1A):A197, 1965.

[27] Jong Uk Kim, Sori Lee, Seung Ji Kang, and Tae-il Kim. Materials and design of nanostructured broadband light absorbers for advanced light-to-heat conversion. *Nanoscale*, 10(46):21555–21574, 2018.

[28] Qiaomei Chen, Zhiqiang Pei, Yanshuang Xu, Zhen Li, Yang Yang, Yen Wei, and Yan Ji. A durable monolithic polymer foam for efficient solar steam generation. *Chemical science*, 9(3):623–628, 2018.

[29] Zhengqi Liu, Long Liu, Haiyang Lu, Peng Zhan, Wei Du, Mingjie Wan, and Zhenlin Wang. Ultra-broadband tunable resonant light trapping in a two-dimensional randomly microstructured plasmonic-photonic absorber. *Scientific reports*, 7:43803, 2017.

[30] Jie Yang, Guo-Qiang Qi, Li-Sheng Tang, Rui-Ying Bao, Lu Bai, Zheng-Ying Liu, Wei Yang, Bang-Hu Xie, and Ming-Bo Yang. Novel photodriven composite phase change materials with bioinspired modification of bn for solar-thermal energy conversion and storage. *Journal of Materials Chemistry A*, 4(24):9625–9634, 2016.

[31] Sarah Madeline Fothergill, Caoimhe Joyce, and Fang Xie. Metal enhanced fluorescence biosensing: From ultra-violet towards second near-infrared window. *Nanoscale*, 10(45):20914–20929, 2018.

[32] NE Stankova, PA Atanasov, Ru G Nikov, RG Nikov, NN Nedyalkov, TR Stoyanchov, N Fukata, KN Kolev, EI Valova, JS Georgieva, et al. Optical properties of polydimethylsiloxane (pdms) during nanosecond laser processing. *Applied Surface Science*, 374:96–103, 2016.

[33] K Kustanovich, V Yantchev, V Kirejev, GDM Jeffries, T Lobovkina, and A Jesorka. A high-performance lab-on-a-chip liquid sensor employing surface acoustic wave resonance. *Journal of Micromechanics and Microengineering*, 27(11):114002, 2017.

[34] Kenneth T Kotz, Wenzong Xiao, Carol Miller-Graziano, Wei-Jun Qian, Aman Russom, Elizabeth A Warner, Lyle L Moldawer, Asit De, Paul E Bankey, Brianne O Petritis, et al. Clinical microfluidics for neutrophil genomics and proteomics. *Nature medicine*, 16(9):1042, 2010.

[35] Oliver Hofmann, Xuhua Wang, Alastair Cornwell, Stephen Beecher, Amal Raja, Donal DC Bradley, Andrew J Demello, and John C Demello. Monolithically integrated dye-doped pdms long-pass filters for disposable on-chip fluorescence detection. *Lab on a Chip*, 6(8):981–987, 2006.

[36] Christopher L Bliss, James N McMullin, and Christopher J Backhouse. Integrated wavelength-selective optical waveguides for microfluidic-based laser-induced fluorescence detection. *Lab on a Chip*, 8(1):143–151, 2008.

[37] Andreu Llobera, Stefanie Demming, Haakan N Joensson, J Vila-Planas, Helene Andersson-Svahn, and Stephanus Büttgenbach. Monolithic pdms pass-band filters for fluorescence detection. *Lab on a Chip*, 10(15):1987–1992, 2010.

[38] Erdinc Sezgin, Ilya Levental, Satyajit Mayor, and Christian Eggeling. The mystery of membrane organization: composition, regulation and roles of lipid rafts. *Nature reviews Molecular cell biology*, 18(6):361, 2017.

[39] Rob Phillips, Julie Theriot, Jane Kondev, and Hernan Garcia. *Physical biology of the cell*. Garland Science, 2012.

[40] AS Urban, M Fedoruk, MR Horton, JO Radler, Fernando D Stefani, and Jochen Feldmann. Controlled nanometric phase transitions of phospholipid

membranes by plasmonic heating of single gold nanoparticles. *Nano letters*, 9(8):2903–2908, 2009.

[41] Poul M Bendix, S Nader S Reihani, and Lene B Oddershede. Direct measurements of heating by electromagnetically trapped gold nanoparticles on supported lipid bilayers. *ACS nano*, 4(4):2256–2262, 2010.

[42] Haiyan Ma, Pengfei Tian, Josselin Pello, Poul Martin Bendix, and Lene B Oddershede. Heat generation by irradiated complex composite nanostructures. *Nano letters*, 14(2):612–619, 2014.

[43] Haiyan Ma, Poul M Bendix, and Lene B Oddershede. Large-scale orientation dependent heating from a single irradiated gold nanorod. *Nano letters*, 12(8):3954–3960, 2012.

[44] Jesper Tranekjær Jørgensen, Kamilla Norregaard, Pengfei Tian, Poul Martin Bendix, Andreas Kjaer, and Lene B Oddershede. Single particle and pet-based platform for identifying optimal plasmonic nano-heaters for photothermal cancer therapy. *Scientific reports*, 6:30076, 2016.

[45] Lauri Viitala, Saija Pajari, Tatu Lajunen, Leena-Stiina Kontturi, Timo Laaksonen, Paivi Kuosmanen, Tapani Viitala, Arto Urtti, and Lasse Murtomaki. Photothermally triggered lipid bilayer phase transition and drug release from gold nanorod and indocyanine green encapsulated liposomes. *Langmuir*, 32(18):4554–4563, 2016.

[46] Bahaa EA Saleh and Malvin Carl Teich. *Fundamentals of photonics*. John Wiley & Sons, 2019.

[47] Craig F Bohren and Donald R Huffman. *Absorption and scattering of light by small particles*. John Wiley & Sons, 2008.

[48] Thomas G Mayerhöfer, Sonja Höfer, and Jürgen Popp. Deviations from beer's law on the microscale–nonadditivity of absorption cross sections. *Physical Chemistry Chemical Physics*, 21(19):9793–9801, 2019.

[49] Thomas G Mayerhöfer and Jürgen Popp. Beer's law derived from electromagnetic theory. *Spectrochimica Acta Part A: Molecular and Biomolecular Spectroscopy*, 215:345–347, 2019.

[50] Charles E Swenberg and Martin Pope. *Electronic processes in organic crystals and polymers*. Oxford University Press New York, 1999.

[51] Terho Kololuoma, JAI Oksanen, P Raerinne, and JT Rantala. Dye-doped solgel coatings for near-infrared laser protection. *Journal of Materials Research*, 16(8):2186–2188, 2001.

[52] Ramprasad Misra and Shankar P Bhattacharyya. *Intramolecular Charge Transfer: Theory and Applications*. John Wiley & Sons, 2018.

[53] Meera Stephen, Kristijonas Genevičius, Gytis Juška, Kestutis Arlauskas, and Roger C Hiorns. Charge transport and its characterization using photo-celiv in bulk heterojunction solar cells. *Polymer International*, 66(1):13–25, 2017.

[54] Juergen Fabian, Hiroyuki Nakazumi, and Masaru Matsuoka. Near-infrared absorbing dyes. *Chemical Reviews*, 92(6):1197–1226, 1992.

[55] Yunus Cengel. *Heat and mass transfer: fundamentals and applications*. McGraw-Hill Higher Education, 2014.

[56] Edwin Kalb, Sammy Frey, and Lukas K Tamm. Formation of supported planar bilayers by fusion of vesicles to supported phospholipid monolayers. *Biochimica et Biophysica Acta (BBA)-Biomembranes*, 1103(2):307–316, 1992.

[57] Ilja Czolkos, Bodil Hakonen, Owe Orwar, and Aldo Jesorka. High-resolution micropatterned teflon af substrates for biocompatible nanofluidic devices. *Langmuir*, 28(6):3200–3205, 2012.

[58] Say Hwa Tan, Nam-Trung Nguyen, Yong Chin Chua, and Tae Goo Kang. Oxygen plasma treatment for reducing hydrophobicity of a sealed polydimethylsiloxane microchannel. *Biomicrofluidics*, 4(3):032204, 2010.

[59] Dhananjay Bodas and Chantal Khan-Malek. Hydrophilization and hydrophobic recovery of pdms by oxygen plasma and chemical treatment—an sem investigation. *Sensors and Actuators B: Chemical*, 123(1):368–373, 2007.

[60] Jennifer S Hovis and Steven G Boxer. Patterning and composition arrays of supported lipid bilayers by microcontact printing. *Langmuir*, 17(11):3400–3405, 2001.

[61] KM Rifat Faysal, June S Park, Jonny Nguyen, Luis Garcia, and Anand Bala Subramaniam. Lipid bilayers are long-lived on solvent cleaned plasma-oxidized poly (dimethyl) siloxane (ox-pdms). *PloS one*, 12(1):e0169487, 2017.

[62] Howard C Berg. *Random walks in biology*. Princeton University Press, 1993.

[63] W Rawicz, KC Olbrich, T McIntosh, D Needham, and E Evans. Effect of chain length and unsaturation on elasticity of lipid bilayers. *Biophysical journal*, 79(1):328–339, 2000.

[64] John R Silvius. Thermotropic phase transitions of pure lipids in model membranes and their modifications by membrane proteins. *Lipid-protein interactions*, 2:239–281, 1982.

[65] Steven T Yang, Manyalibo J Matthews, Selim Elhadj, Diane Cooke, Gabriel M Guss, Vaughn G Draggoo, and Paul J Wegner. Comparing the use of mid-infrared versus far-infrared lasers for mitigating damage growth on fused silica. *Applied Optics*, 49(14):2606–2616, 2010.

[66] John H Koschwanez, Robert H Carlson, and Deirdre R Meldrum. Thin pdms films using long spin times or tert-butyl alcohol as a solvent. *PLoS one*, 4(2):e4572, 2009.

[67] Frederick K Balagaddé, Lingchong You, Carl L Hansen, Frances H Arnold, and Stephen R Quake. Long-term monitoring of bacteria undergoing programmed population control in a microchemostat. *Science*, 309(5731):137–140, 2005.

[68] Mokhtar Mapar, Silver Joemetsa, Hudson Pace, Vladimir P Zhdanov, Bjorn Agnarsson, and Fredrik Hook. Spatiotemporal kinetics of supported lipid bilayer formation on glass via vesicle adsorption and rupture. *The journal of physical chemistry letters*, 9(17):5143–5149, 2018.

[69] Jessamine Ng Lee, Cheolmin Park, and George M Whitesides. Solvent compatibility of poly (dimethylsiloxane)-based microfluidic devices. *Analytical chemistry*, 75(23):6544–6554, 2003.

[70] TS Radhakrishnan. Thermal degradation of poly (dimethylsilylene) and poly (tetramethyldisilylene-co-styrene). *Journal of applied polymer science*, 99(5):2679–2686, 2006.

[71] Wassef W Nawar. Thermal degradation of lipids. *Journal of agricultural and food chemistry*, 17(1):18–21, 1969.

[72] Margrethe A Boyd and Neha P Kamat. Visualizing tension and growth in model membranes using optical dyes. *Biophysical journal*, 115(7):1307–1315, 2018.

[73] Joseph A Curcio and Charles C Petty. The near infrared absorption spectrum of liquid water. *JOSA*, 41(5):302–304, 1951.

[74] Jerker Widengren and Rudolf Rigler. Mechanisms of photobleaching investigated by fluorescence correlation spectroscopy. *Bioimaging*, 4(3):149–157, 1996.

[75] Lin Guo, Jia Yi Har, Jagadish Sankaran, Yimian Hong, Balakrishnan Kannan, and Thorsten Wohland. Molecular diffusion measurement in lipid bilayers over wide concentration ranges: a comparative study. *ChemPhysChem*, 9(5):721–728, 2008.

[76] Peter Lenz, Caroline M Ajo-Franklin, and Steven G Boxer. Patterned supported lipid bilayers and monolayers on poly (dimethylsiloxane). *Langmuir*, 20(25):11092–11099, 2004.

[77] Alexander Bläßle, Gary Soh, Theresa Braun, David Mörsdorf, Hannes Preiß, Ben M Jordan, and Patrick Müller. Quantitative diffusion measurements using the open-source software pyfrap. *Nature communications*, 9(1):1582, 2018.

[78] Daniel Blumenthal, Leo Goldstien, Michael Edidin, and Levi A Gheber. Universal approach to frap analysis of arbitrary bleaching patterns. *Scientific reports*, 5:11655, 2015.

[79] Hideyuki F Arata, Peter Löw, Koji Ishizuka, Christian Bergaud, Beomjoon Kim, Hiroyuki Noji, and Hiroyuki Fujita. Temperature distribution measurement on microfabricated thermodevice for single biomolecular observation using fluorescent dye. *Sensors and Actuators B: Chemical*, 117(2):339–345, 2006.

[80] Quanbo Jiang, Benoit Rogez, Jean-Benoit Claude, Guillaume Baffou, and Jerome Wenger. Temperature measurement in plasmonic nanoapertures used for optical trapping. *ACS Photonics*, 2019.

[81] Indriati Pfeiffer and Fredrik Höök. Bivalent cholesterol-based coupling of oligonucletides to lipid membrane assemblies. *Journal of the American Chemical Society*, 126(33):10224–10225, 2004.

A
Appendix

The mass spectrum of dye molecules A and B mentioned in section 4.1 is included here in figure A.1. The peaks with highest intensity in both dye molecules A and B are at around 920, which is supposed to match the molar mass of the cation in dye molecule B as illustrated in figure 2.2. Even though more rigorous analytic techniques are required to accurately determine the chemical structure of dye molecule A, one can suggest that the dye molecule A contains the same dication as in dye molecule B, which lead to the resemblance in their absorption properties.

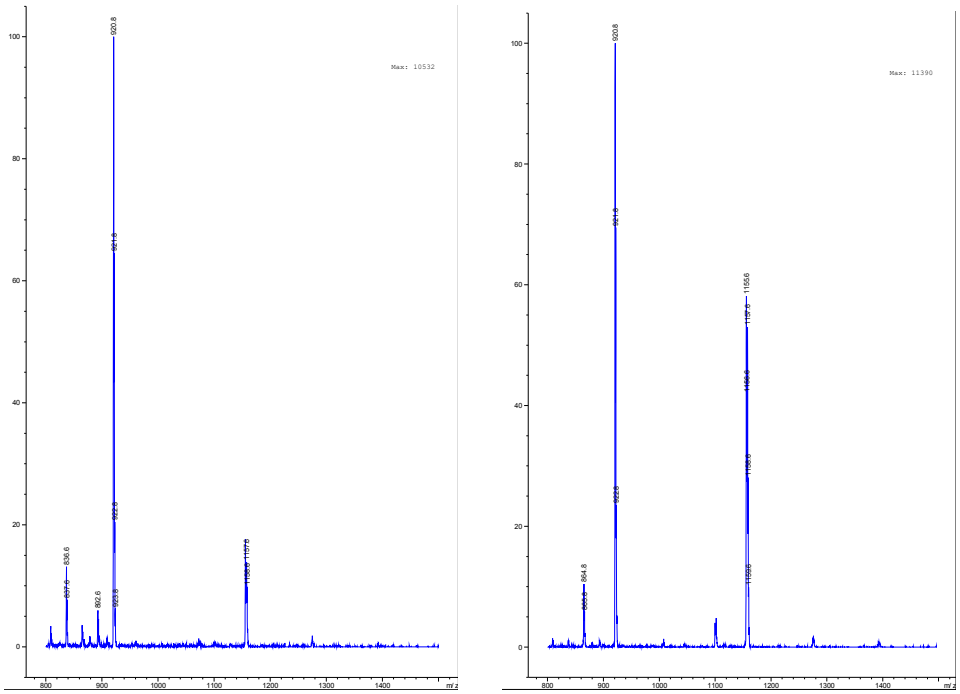

(a) Dye molecule A **(b)** Dye molecule B

Figure A.1: Mass spectrum of NIR dye molecules A and B. The first and second intense peak of dye molecules A and B are at 920 and 1158, respectively.